SEASONAL AND ANNUAL TROPICAL RIVER PATTERN CHANGE DETECTION USING MACHINE LEARNING

Qing LI[1]*, Richard D. WILLIAMS[1], Trevor B. HOEY[2], Brian BARRETT[1], Richard J. BOOTHROYD[1,3]

1. School of Geographical and Earth Sciences, University of Glasgow, Glasgow, UK
2. Department of Civil and Environmental Engineering, Brunel University London, London, UK
3. School of Geography, Earth& Environmental Sciences, University of Birmingham, Birmingham, UK

* Corresponding to: Qing LI, School of Geographical and Earth Sciences, University of Glasgow, Glasgow G12 8QQ, UK.
Email : q.li.2@research.gla.ac.uk ; qingli.ac@gmail.com

ACKNOWLEDGEMENTS

This research is funded jointly by the China Scholarship Council (NO. 201908060049) and the University of Glasgow.

AUTHOR CONTRIBUTIONS

Conceptualization- Q.L., R.W., T.H.; Funding acquisition- Q.L.; Methodology- Q.L., R.W., T.H., B.B.; Investigation- Q.L.; Software- Q.L.; Visualisation- Q.L., R.B.; Supervision- R.W., T.H., B.B.; Writing – initial draft- Q.L.; Writing – reviewing and editing- R.W., R.B., T.H., Q.L., B.B..

PRE-PRINT STATEMENT

This paper is a non-peer reviewed preprint submitted to EarthArXiv. This paper has been submitted to the Earth Surface Processes and Landforms (ESPL) journal for peer review.

CONFLICT OF INTEREST DISCLOUSURE

The authors certify that they have no conflict of interest in the subject matter or materials discussed in this manuscript.

DATA AVAILABILITY STATEMENT

Data are available after peer-review.

Seasonal and annual tropical river pattern change detection using machine learning

Abstract

Rivers in the tropics are more likely to exhibit seasonal changes in pattern than those in temperate regions because of strongly seasonal rainfall. However, such changes in seasonal tropical river patterns have not been widely investigated. Machine learning methods are used in this study with Sentinel-2 multispectral remote sensing images to classify active channel landforms (water; unvegetated bars; vegetated bars) of the Bislak, Laoag and Abra Rivers, north-west Luzon, the Philippines. River patterns are classified five or six times per year from 2016 to 2020. Spatial and temporal trends were investigated, in the context of the rivers' active width, valley confinement, tectonic setting and precipitation. Results show a variety of relationships between each landform unit and active width, but a strong correlation was shown between active width and vegetation area in dry and wet seasons. Rivers were divided into sub-reaches based on observed patterns of water frequency and confinement; Ensemble Empirical Mode Decomposition (EEMD) was then used to decompose the landform time series and precipitation record. EEMD indicates that water and vegetated bars commonly show synchronised fluctuations with precipitation, while unvegetated bars have an anti-phase oscillation with precipitation. It also suggests that deviations from periodic consistency in river pattern may reflect the influence of extreme events and/or human disturbance. At the river system scale, faults perpendicular to the channel centreline were associated with an increase in vegetated bar stability. Overall, the interplay of faults, elevation, confinement and tributary locations impact landform stability. This investigation demonstrates that in tropical regions river pattern should be considered as a dynamic entity as characterising pattern from a single time period may misrepresent a river's character. EEMD is also demonstrated to be an appropriate statistical technique in geomorphology to decompose datasets that are generated from contemporary applications of machine learning to remotely sensed imagery.

Keywords: river pattern change, seasonality, machine learning classification, Ensemble Empirical Mode Decomposition (EEMD), landform stability

1. INTRODUCTION

River channel pattern is a function of a variety of factors including longitudinal gradient, stream power, transport capacity, and bank strength (Buffington & Montgomery, 2022; Church, 2006; Kondolf, Piégay, Schmitt, & Montgomery, 2016). Previous studies on river pattern classification (Demarchi, Bizzi, & Piegay, 2017; Ham & Church, 2012; Horacio, Ollero, & Perez-Alberti, 2017) have been typically approached from a temporally static perspective, focusing on categorising planform at low flow. Whilst this approach is adequate for many meandering rivers in temperate regions, in other climate settings, the aerial proportions of water, exposed sediment and vegetation, which comprise the planform of a river, may substantially vary through a year (Ashworth and Lewin, 2014). This is particularly pertinent for multi-channel rivers in tropical and sub-tropical climates, where rivers are strongly influenced by rapid vegetation growth rates, and significant seasonal variation in flows due to storms and typhoons (Syvitski, Cohen, Kettner, & Brakenridge, 2014). In addition, channel pattern may vary in response to variations in sediment supply from, for example, landslides (Abanco, Bennett, Matthews, Matera, & Tan, 2021) and volcanic events (Gran & Montgomery, 2005) or autogenic adjustments (Paola, 2017). In the last decade, archives of satellite imagery of a sufficiently high spatial resolution to map channel pattern have become available at a temporal frequency that enables inter- and intra-annual mapping (Boothroyd, Williams, Hoey, Barrett, & Prasojo, 2021). This creates opportunities to investigate the spatial and temporal patterns of tropical rivers, which are characterised by a variety of channel forms (Latrubesse et al., 2005). To this end, here, we focus on assessing the multi-temporal dynamics of channel pattern for a set of three rivers in the Philippines. In doing so, we expand the representation of these relatively under-investigated tropical river systems (Dingle et al., 2019) in our global scale understanding of river pattern dynamics.

A variety of multi-temporal investigations have demonstrated how the fundamental fluvial landforms that define river pattern can be mapped from historical airborne and satellite imagery archives, typically by digitising and then quantifying the extent of water, unvegetated bars and vegetated bars (Corenblit, Vautier, Gonzalez, & Steiger, 2020; Dingle et al., 2019; Hajdukiewicz & Wyzga, 2019; Hooke, 2022; Mandarino, Maerker, & Firpo, 2019; Reid & Brierley, 2015; Saleem et al., 2020). For example, Serlet et al. (2018) manually digitised water, unvegetated bars and vegetated bars in a channelised regulated river, from a set of aerial images that covered 80 years, to investigate the co-evolution of alternate bars and vegetation along a 33 km long reach of the temperate, anthropogenically impacted Isère River, France. Whilst manual digitisation of maps and aerial imagery has been widely used to investigate the temporal and spatial dynamics of fluvial systems, including river pattern change, this approach is time consuming and potentially less objective than automated approaches.

Machine learning (Jordan & Mitchell, 2015) has been widely applied to automate landcover classification using remotely sensed satellite data, using both conventional (e.g., pixel- and object-based machine learning strategies) and deep learning (e.g., convolutional neural network) approaches (Phiri et al., 2020; Prakash, Manconi, & Loew, 2020). With respect to conventional approaches, a variety of algorithms are commonly used, including Logistic Regression (LR), Support Vector Machines (SVM), Random Forests (RF) and Artificial Neural Networks (ANN) (Holden, Saito, & Komura, 2016; Ohsaki et al., 2017; Schneider & Guo, 2018). In fluvial geomorphology, SVM has been demonstrated to perform well to classify fluvial landforms (De Luca et al., 2019; Demarchi, Bizzi, & Piegay, 2016) but there are still few large scale or multi-temporal examples to achieve a widely operative, objective framework for consistent river system characterisation (Gurnell et al., 2016).

To reap the benefits of analysing multi-temporal channel pattern data, an integration of spatial and temporal analysis is needed. However, existing practices mostly lack temporal statistical analysis of spatial series. Saleem et al.'s (2020) quantification of planimetric channel changes along a 112 km reach of the tropical River Padma, Bangladesh, for ten timesteps during a 100-year period is a typical example; whilst changes in landform patterns are quantified, they aren't analysed statistically. Whilst overlaying maps of different time periods is an intuitive and straightforward approach to present spatial-temporal changes, this approach is not suitable for big spatial-temporal data analysis. Rather, a statistical temporal analysis is needed to enable quantitative analysis of river system dynamics. One method with potential to achieve this is Ensemble Empirical Mode Decomposition (EEMD), which has been developed to undertake time series analysis in a variety of scientific fields (N. E. Huang et al., 1998; Ridder, 2011; C. Wang & Zhang, 2020), without requiring that the data are stationary. This method decomposes time series into several constituent components, each of which has a corresponding timescale, and a trend. Xu, Liu, Lin, Jiao, and Gong (2019) employed EEMD to decompose vegetation indices from remote sensing imagery and temperature series, then investigated relationships between vegetation change and climate change. This demonstrates how EEMD can be applied to investigate earth observation data, which inspired the use of EEMD to decomposing landform time series in our investigation.

In this paper, we apply a machine learning workflow (Q. Li, Barrett, Williams, Hoey, & Boothroyd, 2022) to rapidly and objectively classify multi-temporal fluvial landforms from the mountain front to the coast for the tropical Bislak, Laoag and Abra Rivers in north-west Luzon, the Philippines. The resulting dataset is then used to investigate four research questions: (1) What are the impacts of channel setting (i.e., active width, catchment size, confinement, tributaries, elevation) on landform (water, unvegetated bars, vegetated bars) patterns? (2) How do landform areas and proportions vary spatially along each river? (3) What are the seasonal patterns in these landform distributions, how consistent are they across the three rivers, and what drives these patterns? (4) What multi-year temporal trends are there in landform area across the sub-reaches of each river, and how do these relate to precipitation patterns?

2. STUDY AREA

Our investigation focuses upon three gravel-bed rivers in north-west Luzon, the Philippines: the Bislak, Laoag and Abra Rivers (Figure 1). For each river, the riverscape that was analysed included the river network in each catchment from the coast to a point upstream where channels were greater than 95% confined on both valley sides. This yielded study lengths of 39, 47 and 82 km, respectively for the Bislak, Laoag and Abra Rivers. Compared to the other two rivers, the Bislak does not have a significant tributary input within the study area (Tolentino et al., 2022). The Laoag has three similar sized tributaries and the Abra has three tributaries with different catchment areas.

The island of Luzon is dominated by sub-tropical East Asian monsoon climate (Liu, Zhao, Colin, Siringan, & Wu, 2009). Tropical cyclones (Cinco et al., 2016) are frequent and cause landslides, flooding and channel change in the region (Abanco et al., 2021; Abon, David, & Pellejera, 2011; Kim, 2019). Notably, more than 50% of tropical cyclone induced rainfall in the Philippines occurs in north-west Luzon (Bagtasa, 2017). In this region, catchments are characterised by strong seasonality of rainfall, with a wet season from May to October and a dry season from November to April. Mean annual rainfall in the Bislak catachment is 2019 mm, with a maximum monthly mean of 546 mm in August (Tolentino et al., 2022). Climate change impacts in west and east Luzon are different; from analysis of 32 years of monthly rainfall distributions, rainfalls measured at all western stations of the Philippines (including stations in the west Luzon) increased (or decreased) synchronously, whereas rainfall fluctuations at eastern stations of the country propagated southward and can be influenced by the winter monsoon, which has long-term variability in the Philippines (Kubota, Shirooka, Matsumoto, Cayanan, & Hilario, 2017). Additionally, an analysis of records from 1901 to 2013 indicated rainfall in north-west Philippines increased around May to June and decreased around October to November (Kubota et al., 2017).

3. DATA AND METHODS

3.1 Sentinel-2 acquisitions

The Sentinel-2 mission comprises a constellation of two identical satellites launched on 23 June 2015 and 7 March 2017. The multispectral instruments (MSI) onboard the pair of satellites enable monitoring of the Earth's land cover typically using 10 m resolution imagery across four spectral bands and/or 20 m imagery across six spectral bands (Korhonen, Hadi, Packalen, & Rautiainen, 2017; Phiri et al., 2020). Sentinel-2's capability of revisiting all continental land surfaces between 56°S and 82.8°N every five days has encouraged many investigations on land cover dynamics of the Earth's surface (Phiri et al., 2020; Sonobe et al., 2018; X. C. Yang, Zhao, Qin, Zhao, & Liang, 2017), including river change (Rabanaque, Martinez-Fernandez, Calle, & Benito, 2022; Spada, Molinari, Bertoldi, Vitti, & Zolezzi, 2018). However, in tropical areas the presence of clouds can substantially reduce the frequency of Sentinel-2 imagery that is suitable for land cover mapping; for the three rivers in this study, imagery acquisitions with good visibility were sometimes spaced two to three months apart. Nevertheless, to investigate the seasonal changes in river patterns, we were able to obtain five or six Sentinel-2 Level-1C (Top-Of-Atmosphere reflectance) acquisitions from the USGS Earth Explorer portal (http://earthexplorer.usgs.gov) for every year between 2016 and 2020 (Figure 2). These acquisitions had less than 5% cloud cover across the channel area and were typically well temporally distributed throughout each year.

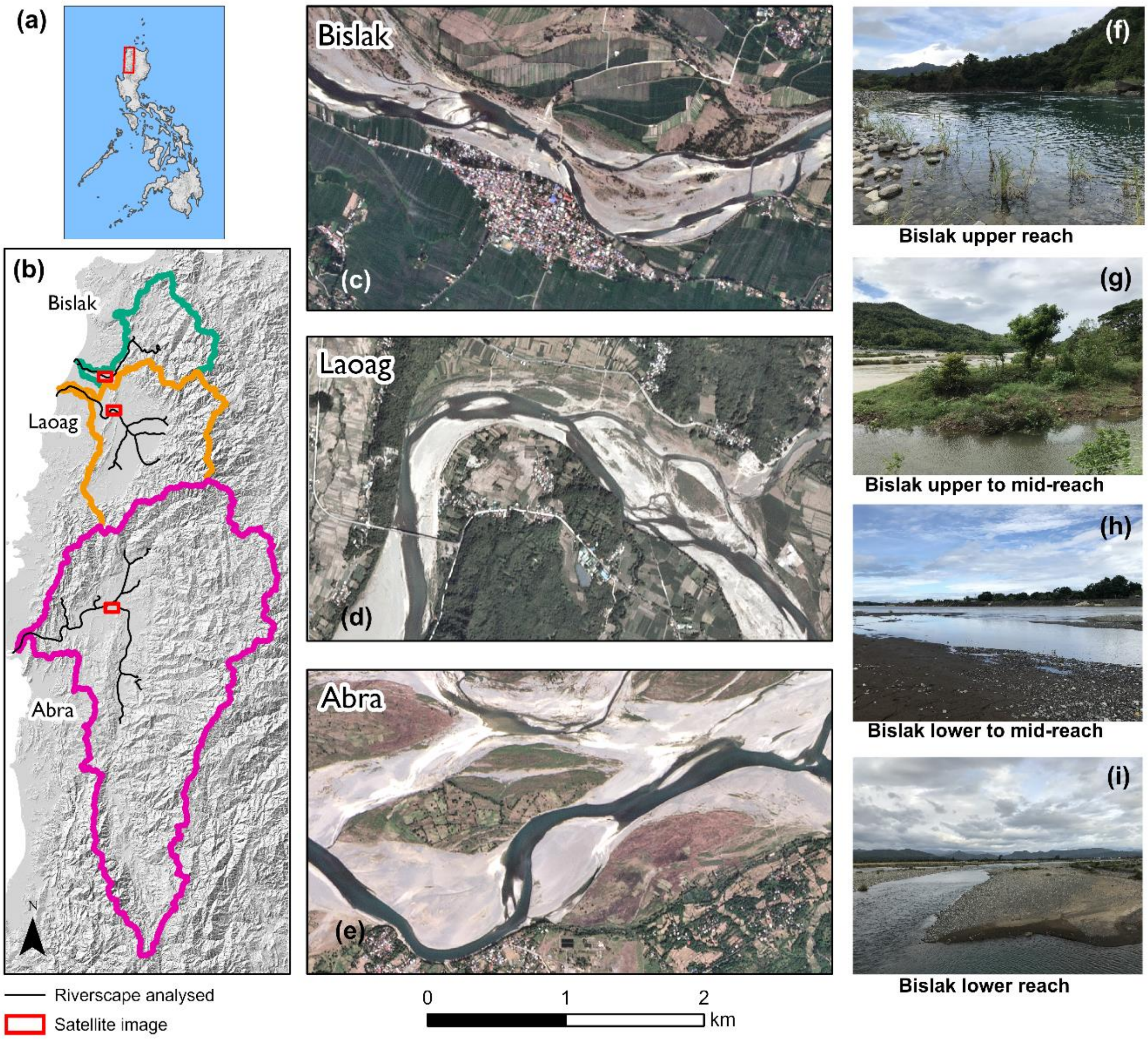

Figure 1. (a) The Philippines; red box is the study area in north-west Luzon shown in (b); (b) The Bislak, Laoag and Abra catchments, with extents of riverscapes that were analysed shown as black lines. (c - e) PlanetScope satellite imagery (dated December 2019) showing representative reaches of each river (image centres: Bislak 18.23 N,120.65 E; Laoag 18.13 N, 120.67 E; Abra 17.63 N, 120.68 E), with extents indicated on (b). (f - i) Oblique photographs of riverscapes along the Bislak River.

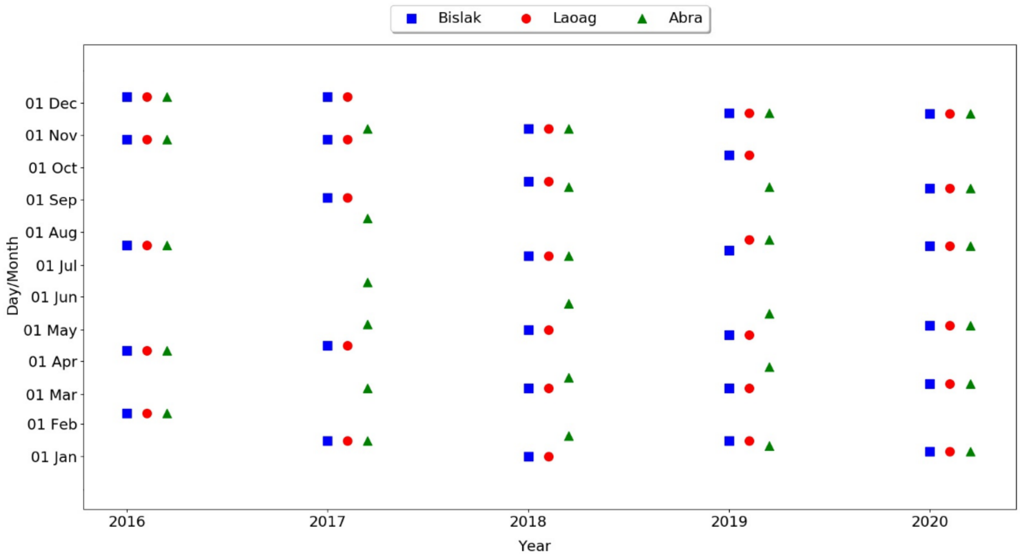

Figure 2 The timing of Sentinel-2 imagery acquisitions used in seasonal change investigations, for the Bislak, Laoag and Abra Rivers.

3.2 Geographic object-based image analysis

Ten bands at resolutions of 10 m and 20 m from Sentinel-2 MSI acquisitions and five environmental indices calculated from the Sentinel-2 data were selected to prepare learning features for image classification. Atmospheric correction was then applied to Sentinel-2 Level-1C products (Top-Of-Atmosphere reflectance) to generate Level-2A products (Bottom-of-Atmospheric reflectance) using the sen2cor processor developed by the European Space Agency (Main-Knorn et al., 2017). Using the Level-2A imagery, the ATPRK image fusion algorithm (Q. M. Wang, Shi, Li, & Atkinson, 2016) was applied to downscale 20 m imagery to 10 m resolution (Q. Li et al., 2022). Subsequently, the five water and vegetation environmental indices were calculated from 10 m bands (including original 10 m bands and downscaled 20 m bands). The five environmental indices were: normalised difference vegetation index (NDVI; Carlson and Ripley, 1997); normalised difference moisture index (NDMI; Wilson and Sader, 2022); normalised difference water index (NDWI; Gao, 1996); modified enhanced vegetation index 1 (MEVI1; Huete et al, 2002); modified enhanced vegetation index 2 (MEVI2; Jiang et al, 2008). As NDMI, MEVI1 and MEVI2 were originally developed for Landsat and MODIS satellite imagery, for Sentinel-2 Level-2A downscaled imagery, indices tended to have values outside of a -1 to 1 range. To maintain bounded conditions (-1 to 1), we added a constant 10^a to the denominator of each of these indices (A. R. Huete, 1988; Ji, Zhang, Wylie, & Rover, 2011). For this case, we tested the constants by giving integers to a. We found a = 4 maintained the range from -1 to 1 for NDMI and MEVI2, while a = 5 maintained the range from -1 to 1 for MEVI1 (Q. Li et al., 2022). Consequently, a set of fifteen 10 m resolution layers were produced for each acquisition. These layers included the Sentinel-2 processed spectral bands, and the water and vegetation environmental indices. The set of layers were segmented into geographical objects (i.e., patches of pixels) using the Large Scale Mean Shift (LSMS) algorithm (Comaniciu & Meer, 2002; Ming, Yang, Li, & Song, 2011), employing open-access Orfeo Toolbox 6.6.1 software.

To bound the segmented geographical objects within the river channel, we generated an active channel extent for each river. We first detected the annual averaged area containing water and unvegetated bars homogeneously within the active channel (Boothroyd et al., 2021). We automatically closed gaps in the annual active channel area caused by vegetated islands using standard image processing techniques. For vegetated bars connected to the active channel, we manually edited the active channel area to include the vegetated bars. In the active channel, the segmented objects were manually allocated into three landform units (water, unvegetated bars and vegetated bars) and no data units (objects obscured by clouds or scattered urban units) to generate the ground truth dataset. Subsequently, these object samples were ready for SVM machine learning. For the machine learning model, the training dataset was built with imagery data of the Bislak River from six dates in 2018; as reported in Q. Li et al. (2022), including imagery from all seasons resulting in a higher model performance than only using data from a single season. The classification model was tested and assessed using overall accuracy (OA), water accuracy (WA), unvegetated bar accuracy (BA) and vegetated bar accuracy (VA). Accuracy was assessed using images of the: Bislak River in 2017 and 2019; Laoag River in 2018; and Abra River in 2019.

3.3 Catchment-averaged accumulated rainfall totals

There is a paucity of ground-based rainfall measurements in north-west Luzon, especially in catchment headwaters. To quantify and compare catchment-averaged accumulated rainfall totals for the periods between Sentinel-2 image acquisitions, we therefore used satellite-derived precipitation data from the Integrated Multi-satellite Retrievals for Global Precipitation Measurement (GPM IMERG) mission. The satellite-derived precipitation estimates have a spatial resolution of 0.1° and a temporal resolution of 30 minutes (Huffman et al., 2019). Across the Philippines, satellite-derived estimates from GPM IMERG show good agreement with ground-based rainfall measurements from synoptic stations and automatic rain gauges but a paucity of ground-based rainfall measurements are reported in the Northern Cordillera mountains (Veloria et al., 2021). We ingested shapefiles for the Abra, Bislak and Laoag catchments into Google Earth Engine and clipped the global GPM IMERG product to each catchment's extent. Due to variation in catchment size and shape, the number of GPM IMERG cell centres varied per catchment (Abra = 66; Bislak = 12; Laoag = 21). We calculated catchment-averaged accumulated rainfall totals (mm) per 10 days for the period between 1 January 2016 and 10 July 2021.

3.4 Ensemble Empirical Mode Decomposition

Time series decomposition was applied to analyse temporal trends in the remote sensing results. Numerous signal decomposition methods have been applied to geomorphic data, many of which require data that are stationary (mean and variance constant over time). Our time series are short and are expected to contain seasonal cycles and potentially longer-term trends, all of which preclude a stationarity assumption. Processing methods for non-stationary data such as spectrograms, wavelets, and the empirical orthogonal function expansion (EOF), each have shortcomings when applied to data from physical measurements (N. E. Huang et al., 1998). An alternative approach, Empirical Mode Decomposition (EMD) has therefore been proposed to process non-stationary and non-linear series into components at different frequencies (N. E. Huang et al., 1998). Using this method, the decomposed component (signal) is referred as the Instinct Mode Function (IMF). Here, we use a derivative of EMD, Ensemble Empirical Mode Decomposition (EEMD), which solves the mode mixing problem encountered in EMD by adding white noise to the signal (Mohguen & Bekka, 2015; Torres, Colominas, Schlotthauer, & Flandrin, 2011). Specifically, EEMD provides a way to decompose our river landform time series which were sampled at unequal time steps due to the availability of cloud-free satellite images.

EEMD was implemented using the PyEMD library in Python v3.6 (Laszuk, 2017). Since EEMD has not been widely used in geomorphology, we illustrate the technique for the Abra River precipitation time series (Figure 3). The same method was applied to precipitation data for the Bislak and Laoag Rivers and to the three river landform data sets. In this analysis, noise width was set to 0.2 and 100 trials were performed (Z. W. N. E. Huang, 2004; Ridder, 2011). The precipitation series was decomposed into five IMFs and one residual series (Figure 3a), where each IMF corresponds to an instantaneous frequency, which is usually interpreted to have physical meaning at a characteristic time scale. The residual can be interpreted as the local mean trend of the original data (N. E. Huang et al., 1998). Figure 3a shows that the mean precipitation for the Abra River catchment has a decreasing trend over the past 5.5 years.

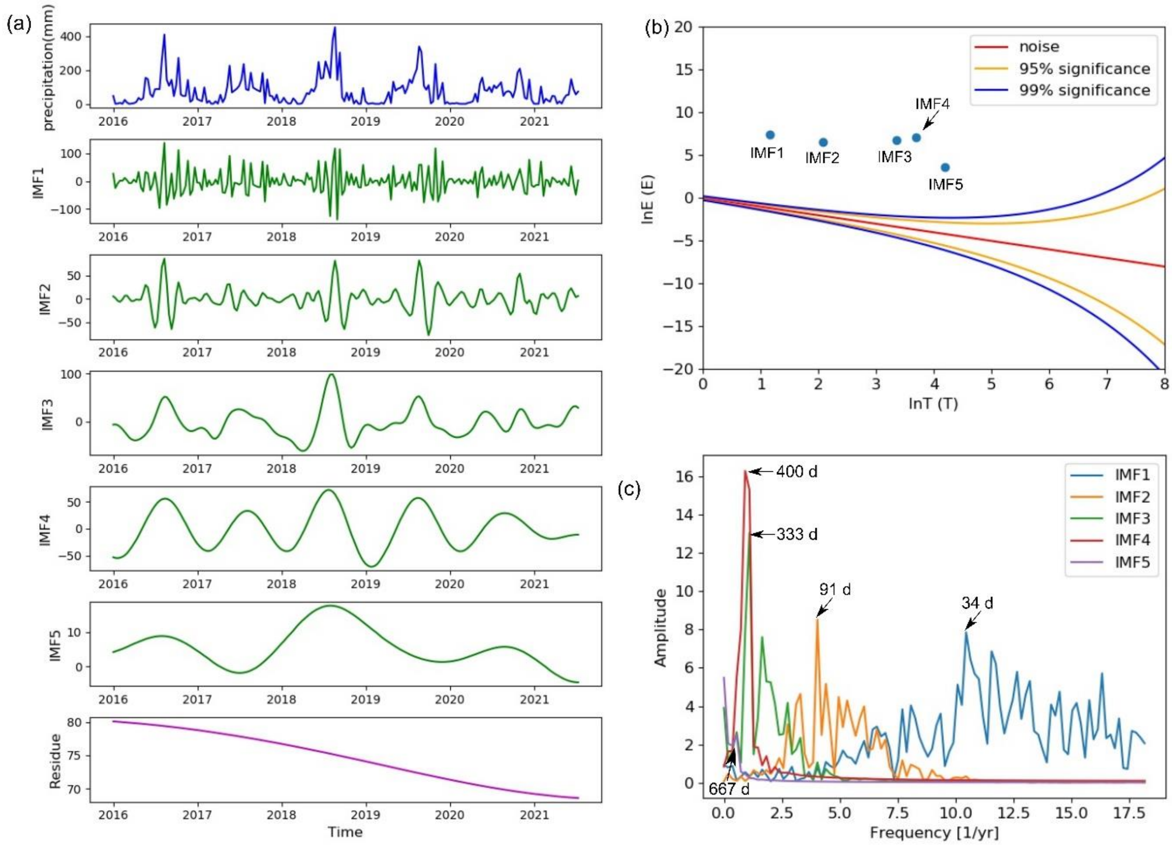

Figure 3. Ensemble Empirical Mode Decomposition (EEMD) on GPM IMERG catchment-averaged (every 10 days) precipitation data from the Abra catchment.
(a) Upper plot (blue) is the precipitation data for the Abra River catchment. The subsequent five plots (green) are decomposed Instinct Mode Functions (IMFs), and the lowest plot (purple) is the residual of the decomposition. (b) The significance of the IMFs, where T = mean period (years) and E = Energy density. The mean period, the energy density for the added noise and confidence bands are calculated using the method of Huang (2004). (c) IMF amplitude in quantity peak as a function of signal frequency from fast Fourier Transformation (Cerna & Harvey, 2000). This shows the dominant frequencies of each IMF, which correspond to the main periods of the decomposed components.

Previous work (Kong, Meng, Li, Yue, & Yuan, 2015) has shown that the highest frequency signal (IMF1) can contain signal noise. To test the significance of all the IMFs, we used Huang's (2004) method for the IMFs and for white noise (Figure 3b). All five IMFs (Figure 3b; blue dots) from the Abra precipitation data are significant (>99% level). To investigate the possible physical meaning of these significant IMFs, the frequency against amplitude plot (Figure 3c) shows the main frequencies (periods) within each IMF. Each IMF contains instantaneous frequencies, so each IMF may be associated with more than one timescale if there are multiple peaks in the frequency series. For example, IMF4 has only one peak at a frequency of 1.09 year (400 days), whereas, the other IMF plots show multiple peaks, that may indicate multiple environmental driving factors within the decomposed component. EEMD results from the precipitation data for both, Bislak and Laoag Rivers also produce single peaks for IMF4 (see supplementary Figure S1 and Figure S2), with an annual period (≈1.09 year), hence IMF can be used to analyse annual precipitation fluctuations. Similarly, IMF2 has a period of 91 days (Figure 3c) and is interpreted as a seasonal fluctuation, the magnitude of which varies considerably between years (Figure 3a). Using the same decomposition method for landform area time series, we compare IMF4 for precipitation with similar frequency (period) for the landform data to identify temporal responses in river landform units to annual precipitation variability.

4. RESULTS

4.1 Machine learning model classification performance

The SVM classification training model was built from six dates of Bislak River imagery, distributed across all seasons in 2018. Table 1 summarises the model's performance for selected years for the three rivers. Overall Accuracy (OA) exceeds 0.86 for all rivers, indicating that the machine learning model has an appropriate efficiency to classify fluvial landforms for rivers in north-west Luzon. Although the recognition efficiency of vegetated bars is lower than that of water and unvegetated bars, Vegetation Accuracy (VA) still exceeds 0.70 for all test cases. To illustrate the classification, Figure 4 presents the classification results across different seasons in 2019, for the Abra River. The spatial distribution of landforms suggests there could be a seasonal cycle of river pattern change; vegetation extent and water cover increased between March and September and decreased between September and January of the next year.

Table 1 Assessment of SVM classification performance for the Bislak, Laoag and Abra Rivers for a selection of years. For each metric, a value of 1.0 would indicate perfect agreement.

River (Year)	Overall Accuracy (OA)	Water Accuracy (WA)	Unvegetated Bar Accuracy (BA)	Vegetated Bar Accuracy (VA)
Bislak (2017)	0.904	0.883	0.981	0.752
Bislak (2019)	0.897	0.868	0.948	0.789
Laoag (2018)	0.866	0.937	0.860	0.735
Abra (2019)	0.872	0.901	0.959	0.721

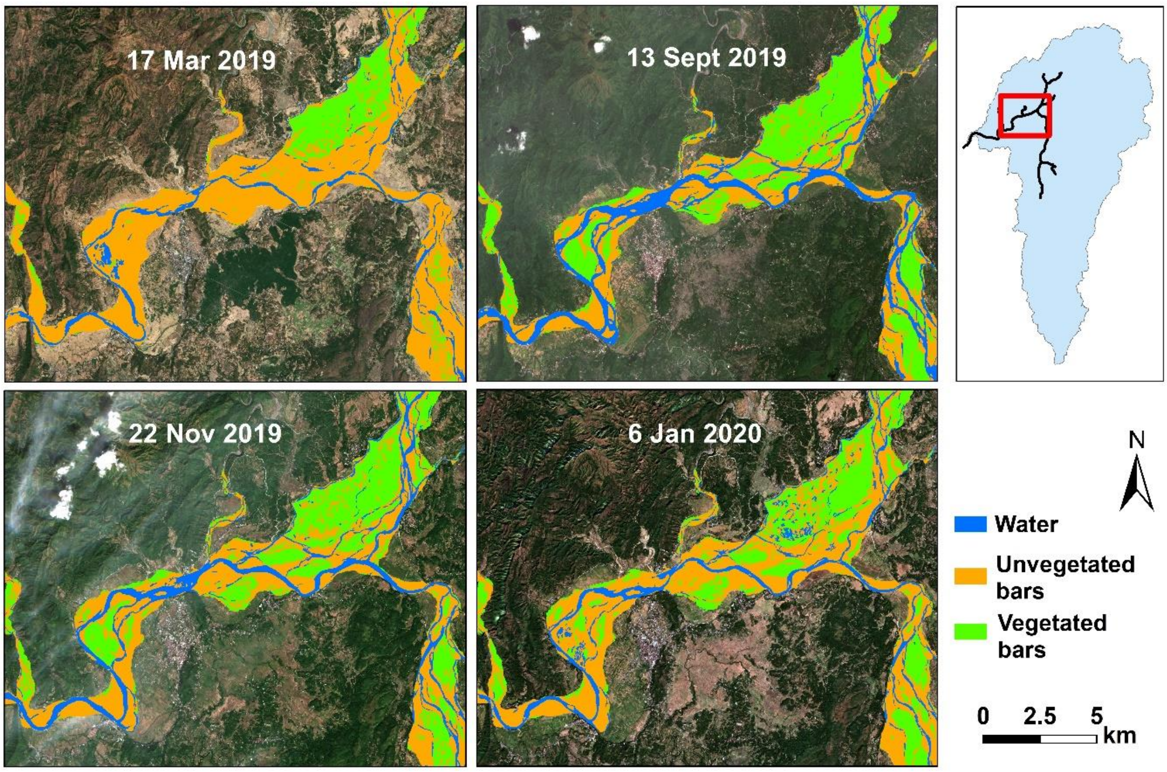

Figure 4. Classified river landforms for a segment of the Abra River during a one-year period. Seasonal variation in landforms is evident during the year.

4.2 River landform classification

Following the acceptable performance of the SVM machine learning model, the model was then applied to classify river landforms for the 5.5 year long imagery dataset, for the three rivers. Figure 5 shows how the proportions of water, unvegetated bars and vegetated bars change longitudinally and temporally. A proportional cover approach is used to show the data because it removes the influence of active width (AW) on observed change. From a spatial perspective, the results show a variety of landform changes from downstream to upstream. In general, for all three rivers, there were higher proportions of vegetated bars for reaches that have greater active widths (AWs). For the Laoag and Abra Rivers, reaches located closer to the sea had greater proportions of water extent relative to mid- and upper reaches. This may be due to the contribution of tributary inflows to these rivers. However, in other ways the Laoag and Abra rivers are different. The lower reach of the Laoag River had a relatively high proportion of vegetation whilst the proportion of bars is relatively low compared to the mid- and upper- reaches. For the mid reach (9 - 32 km from the sea) of the Abra River, the vegetated bars occupied a lower proportion of the reach relative to mid-reaches of the Laoag River. For this reach, the proportion of vegetated and unvegetated bars were relatively similar.

Temporal patterns in landform proportions (Figure 5) were synchronised across the three rivers, showing yearly variation throughout the study area for each river. In general, the proportion of vegetation started to increase after late May and then decreased before early February in the subsequent year. These annual dynamics can also be seen in the mapped landform changes for the Abra River in 2019-2020 (Figure 4). For many reaches, Figure 5 indicates that there were corresponding temporal changes in water proportion. However, for some reaches, there was a slight increase in vegetated bar proportion and a decrease unvegetated bar proportion, whilst the water proportion remained stable. This phenomenon probably indicates seasonal vegetated island development.

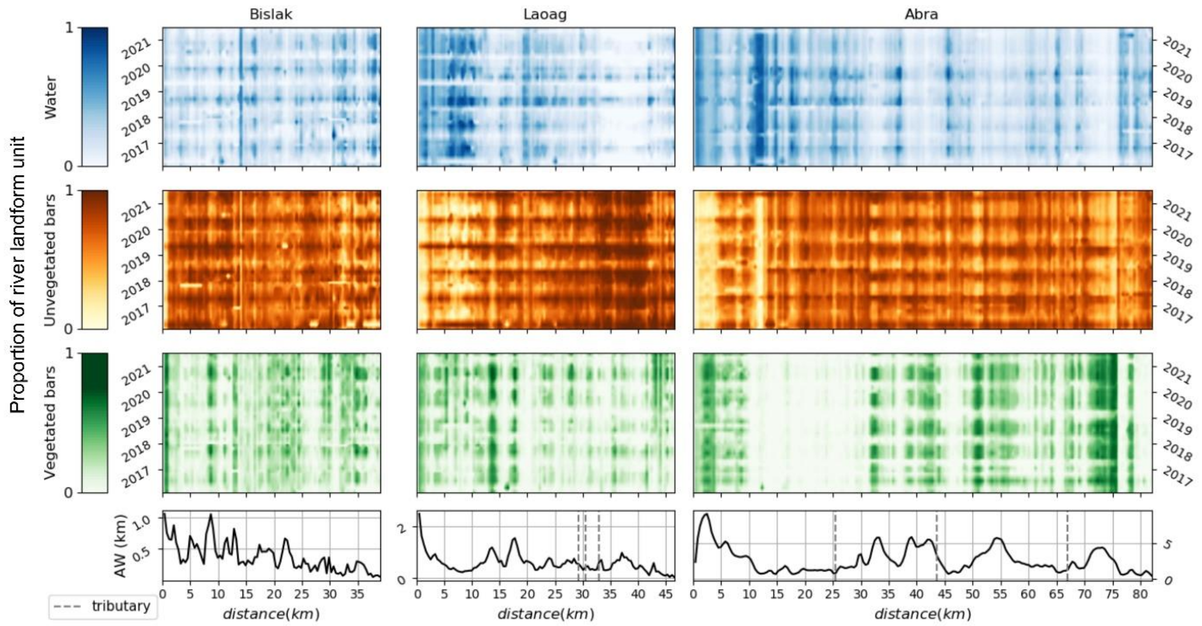

Figure 5 Longitudinal and temporal variation in landform proportions, and active width (AW), of the Bislak, Laoag and Abra rivers between February 2016 and July 2021. Classification maps are available from the digital data supplement (available after peer-review).

To analyse and compare temporal changes in landform pattern from a spatial perspective, the three rivers were segmented into sub-reaches based on water frequency and river confinement. Figure 6 and Figure 7 shows five-year water frequency maps for the Bislak, Laoag and Abra Rivers, together with contextual information on topography, fault lines (PHIVOLCS, 2015) and confinement. Confinement was assessed by overlaying the active channel extent with the mapped valley floors. Valley floors were manually mapped in GIS using a nationwide DEM (Grafil & Castro, 2014). We defined the valley margins morphologically, by identifying breaks in slope from relatively flat, low elevation areas to relatively steep hillslopes. Segment divisions were set when: (i) the water frequency map showed a change in river pattern from multi-thread to single thread, or vice-versa; (ii) there was a change from unconfined to confined valley, when over 90% of the proportion of the river was confined on both banks; and (iii) there were confluences. The Bislak, Laoag and Abra Rivers were segmented into 9, 10, and 16 sub-reaches respectively.

Figure 6 shows that faults in the study region, and thus geological structure and position of high ground, are generally oriented north to south, Thus, rivers would typically flow along this approximate axis. An example from the Bislak River (Figure 6a) provides a view of river cutting through the high ground to reach sea (base) level to the immediate west. As rivers can incise at about the same rate as mountain uplift (often about 1mm/year) (Maxwell et al., 2018), incised meanders in the Bislak River provide evidence for river downcutting during uplift. Sub-reach 7 and 8 of the Bislak River might be a graben with faults on both sides where the hills are uplifting and the basin in the middle is subsiding.

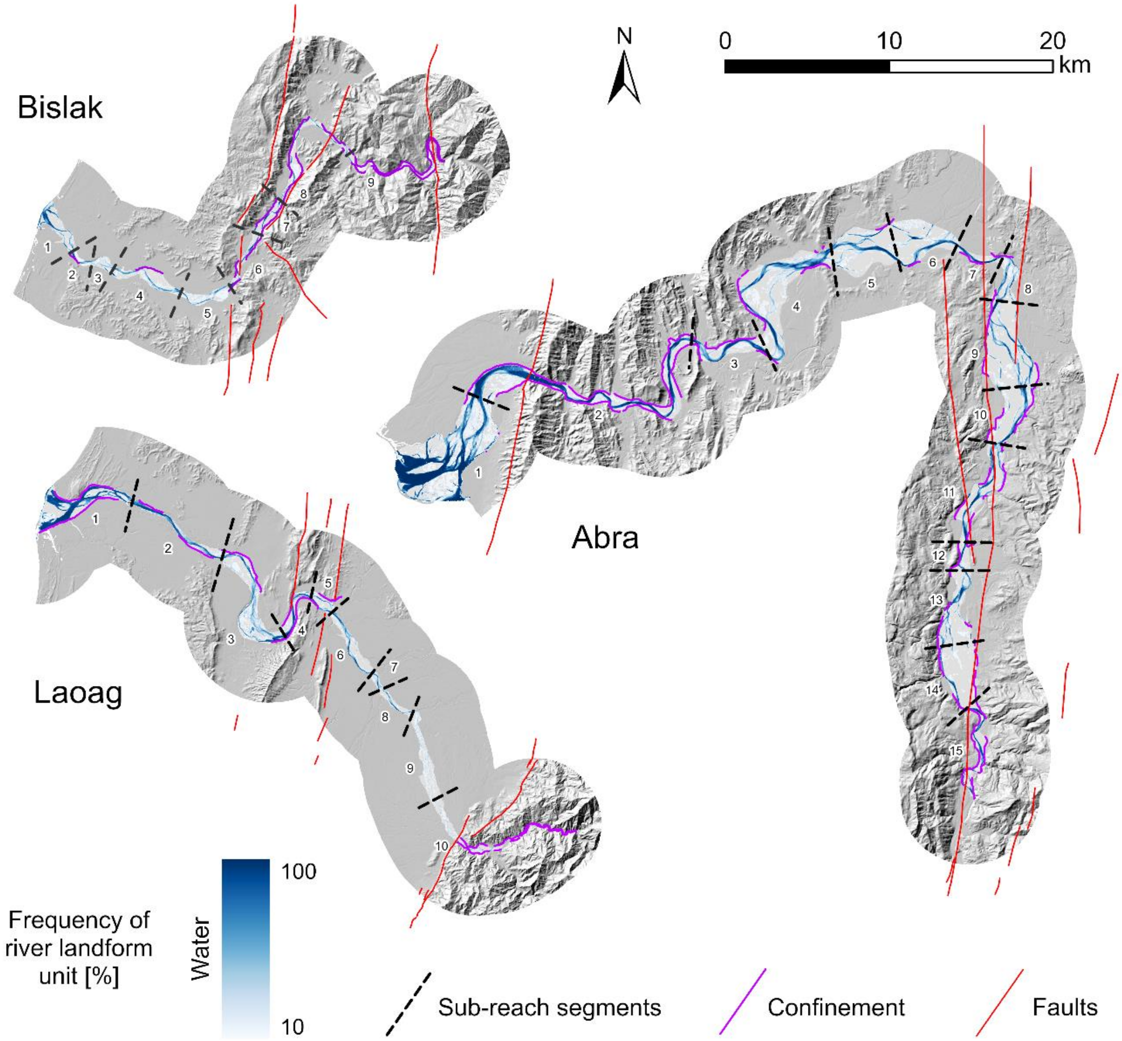

Figure 6. River segmentation of the Bislak, Laoag and Abra Rivers.

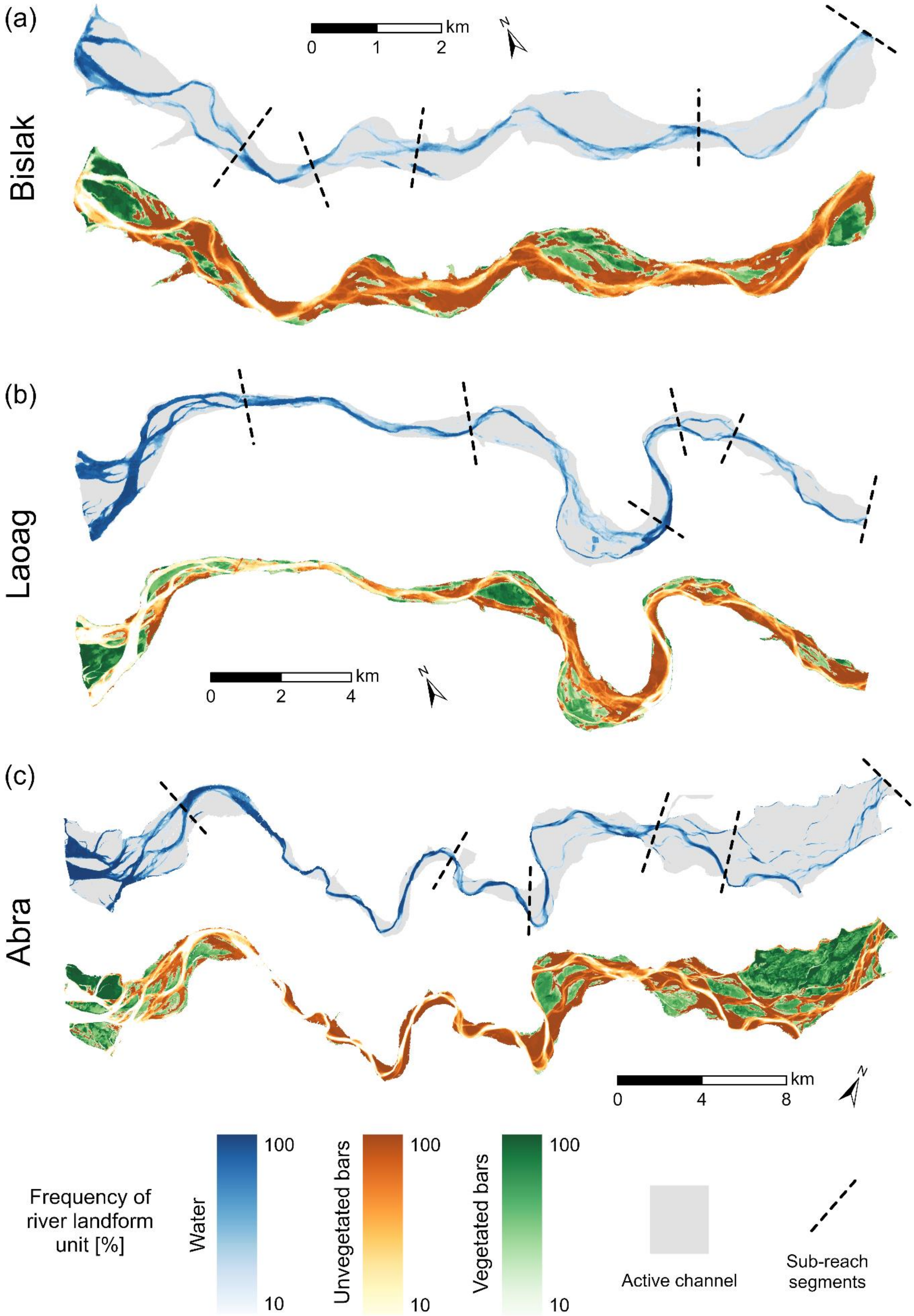

Figure 7. Landform frequency maps for the (a) Bislak, (b) Laoag and (c) Abra Rivers.

4.3 Active width impacts on area and proportion of landforms

To examine the potential relationships between active width (AW) and the three landforms, mean values of area and proportion in the dry and wet season were investigated for the three rivers, using data from each river segment (Table 2). Results for the areal analysis of the Abra River are shown in Figure 8 whilst results from the proportional analysis for the Laoag River are shown in Figure 9. Supplementary figures (S3 to S6) show the results for the other area and proportion combinations for the three rivers. Correlation coefficients were calculated between AW and mean landform area/proportion, for dry and wet seasons. Figures S7 to S12 present the correlation coefficients for the five-year duration time series, from February 2016 to November 2020. Overall, the data in Figures 8 to 9, and S3-S12, enable both spatial and temporal trends in the relationship between AW and landforms to be investigated; these are considered in turn in the next two sub-sections.

With respect to landform area (Table 2, Figure 8b, S3 and S4), there are positive correlations between the three landforms and AW across all three rivers ($Area_{water}$ < $Area_{veg}$ < $Area_{bars}$ in the Bislak River, generally $Area_{water}$< $Area_{bars}$< $Area_{veg}$ in the Laoag and the Abra Rivers). Water area is moderately impacted by AW in this region. This contrasts to vegetation and bars, which are strongly controlled by AW. The results also indicate that the strength of the correlation between AW and vegetation area perhaps relates to river catchment spatial scale, since the coefficient values of AW-$Area_{veg}$ in the three rivers increases with catchment size. In addition to relationships between landforms and AW, $Area_{veg}$ and $Area_{water}$ also have a significant moderate correlation (0.71 in Bislak River; 0.64 in Laoag River; 0.61 in Abra River) in dry season.

For proportional analysis (Table 2, Figure 9b and S5, S6), only $Prop_{veg}$ in Abra River has a moderately high and significant correlation with AW (>0.60 in both dry and wet seasons). The correlation between $Prop_{veg}$ and AW in the Laoag and Bislak Rivers were both significant weak positive (<0.6), with the coefficient in Bislak River lower than that in Laoag River. For this case, the spatial scale of the river probably also has an impact on the correlations between vegetation proportion and active width in the region; this is an example of the river scale impacts on vegetation area and active width that were discussed above. For the Bislak and Laoag River, no high or moderate correlation coefficients (≥0.6 or ≤-0.6) between $Prop_{landform}$ (any landform proportion) and AW were observed. However, during the dry season, across all three rivers, $Prop_{water}$ and $Prop_{bars}$ all had a strong significant negative correlation (≤-0.7). Moreover, in the wet season of Laoag River, $Prop_{water}$ and $Prop_{bars}$ had a strong significant negative correlation (-0.79), which is different from the other two rivers. Additionally, $Prop_{veg}$ and $Prop_{bars}$ had negative correlations (<-0.6) in the Bislak River for both seasons; in the Laoag River, a negative correlation (-

0.64) only occurred in the dry season. By contrast, for the Abra River, there was only a weak negative correlation (-0.47) between $Prop_{veg}$ and $Prop_{bars}$.

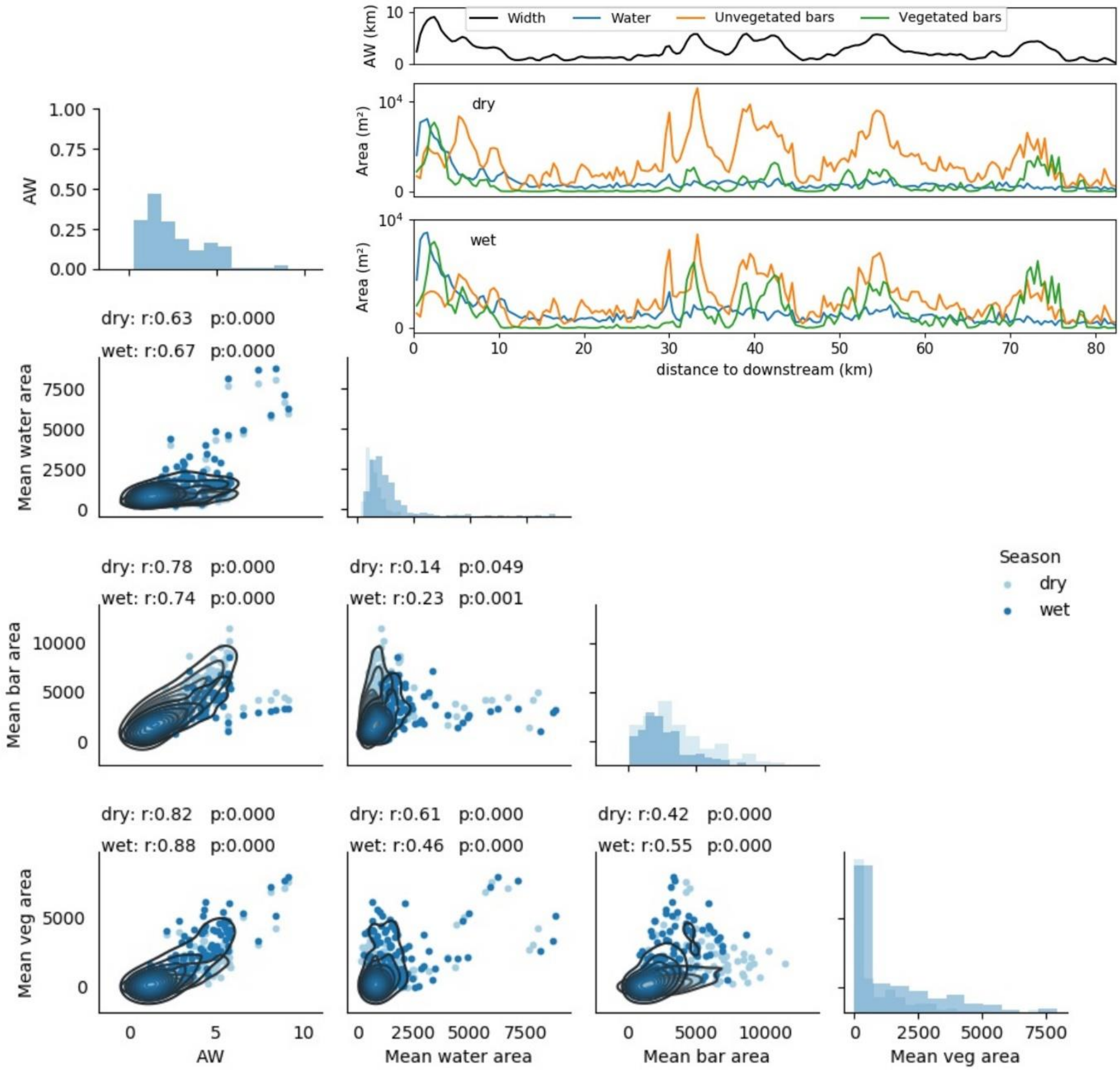

Figure 8 (a) Longitudinal trend in active width (AW) and mean area of three landforms (water, unvegetated bars, vegetated bars) for the Abra River, for wet and dry seasons. (b) Matrix plots to represent correlations between mean values of landform areas and AW. Histograms illustrate mean value distributions at equal spaced spatial distance along the river. Kernel distribution estimation is shown using contour plots. Tables above each matrix plot summarise correlation coefficients (r) and associated statistical significance (p) between landform areas and AW in wet season and dry season.

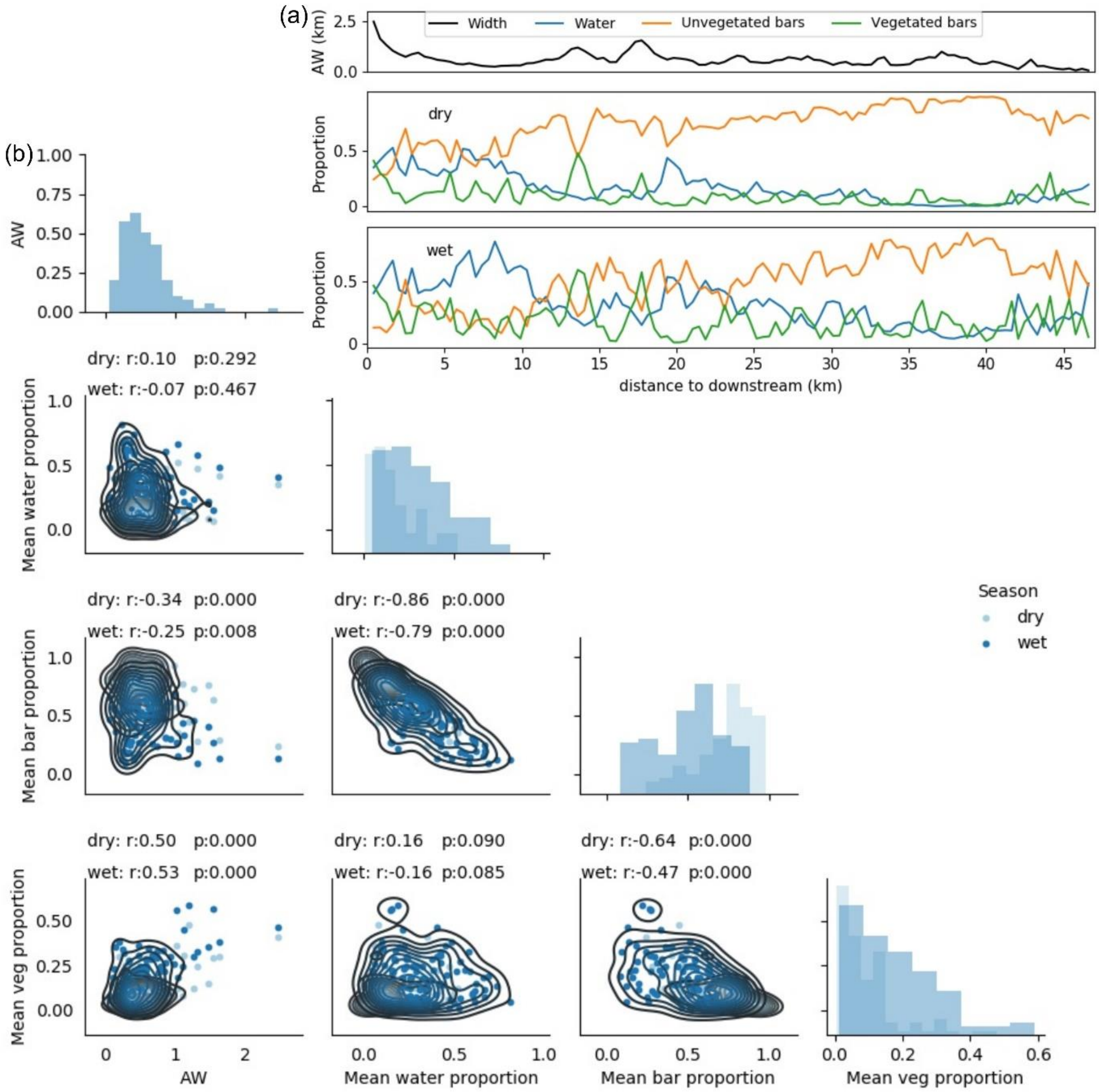

Figure 9 (a) Longitudinal trend in active width (AW) and mean proportion of three landforms (water, unvegetated bars, vegetated bars) for the Laoag River, for wet and dry seasons. (b) Matrix plots to represent correlations between mean values of landform proportions and AW. Histograms illustrate mean value distributions at ~410 m spatial distance along the river. Kernel distribution estimation is shown using contour plots. Tables above each matrix plot summarise correlation coefficients (r) and associated statistical significance (p) between landforms proportion and AW in wet season and dry season.

Table 2 Correlations between landforms and active width (AW) for the Bislak, Laoag, Abra Rivers for wet and dry seasons. r refers to correlation coefficient, where r≥ 0.60, text is bold. p refers to significance.

Approach	River	Season	Water-AW		Bar-AW		Veg-AW	
			r	p	r	p	r	p
Area	Bislak	Dry	0.46	<0.001	**0.86**	<0.001	**0.67**	<0.001
		Wet	**0.60**	<0.001	**0.78**	<0.001	**0.76**	<0.001
	Laoag	Dry	**0.64**	<0.001	**0.73**	<0.001	**0.81**	<0.001
		Wet	**0.69**	<0.001	0.50	<0.001	**0.86**	<0.001
	Abra	Dry	**0.63**	<0.001	**0.78**	<0.001	**0.82**	<0.001
		Wet	**0.67**	<0.001	**0.74**	<0.001	**0.88**	<0.001
Proportion	Bislak	Dry	-0.45	<0.001	0.18	0.087	0.31	0.002
		Wet	-0.41	<0.001	-0.09	0.404	0.42	<0.001
	Laoag	Dry	0.10	0.292	-0.34	<0.001	0.50	<0.001
		Wet	-0.07	0.467	-0.25	0.008	0.53	<0.001
	Abra	Dry	-0.24	0.001	-0.17	0.014	**0.61**	<0.001
		Wet	-0.35	<0.001	-0.32	<0.001	**0.65**	<0.001

The above analysis indicates that the relationship between AW and each of the three landforms varies between wet and dry seasons. To further investigate this relationship, from a temporal perspective, we selected the combinations that had above moderate correlation (>0.6). Then we calculated the correlation coefficients for specific dates, instead of using mean values for the wet and dry seasons, with the objective of minimising the temporal range of significant high correlations. The results are shown for the three rivers in Figures S7-S12, for area and proportion respectively. The correlation between $Area_{\mathrm{veg}}$ and AW was commonly high for the three rivers. Specifically, vegetation area shows higher correlation to the AW in the wet season compared to that in the dry season. However, for each river, the first dry date was always associated with a high correlation between $Area_{\mathrm{veg}}$ and AW, indicating there is a lag in AW impacts on vegetation area. The strongest correlations between AW and $Area_{\mathrm{veg}}$ occurred from early July to early December every year. The AW correlations to $Area_{\mathrm{bar}}$ were also similar for the three rivers. However, for the Bislak and Laoag Rivers, $Area_{\mathrm{bar}}$ was overall more synchronised with AW in the dry season. Beyond relationships with *Area*, the proportional analysis showed that the increase in $Prop_{\mathrm{water}}$ corresponded to a significant decrease in $Prop_{\mathrm{bar}}$ across all three rivers in dry season but for the Bislak River only in the wet season. This may be due to the lower proportion of vegetation growing in the wet season in the Bislak River. Besides, late January to mid-March contributed the strongest correlation between $Prop_{\mathrm{water}}$ and $Prop_{\mathrm{bar}}$. This period could also be regarded as the time period in which vegetation has the least impact on the channel. Additionally, the correlations between $Prop_{\mathrm{veg}}$ and $Prop_{\mathrm{bar}}$ in the Laoag River are moderate to high from April to June, whilst these correlations for the Bislak River varied across the five years. The reason of this difference between these two rivers could not be determined.

4.4 Temporal changes in sub-reach landforms

Temporal patterns in landform areas across the sub-reaches of each river were assessed using the EEMD to decompose time series of classified water, unvegetated bar and vegetated bar areas. Data for at least 32 dates covering >5.5 years were used. As noted in section 3.4, the IMF4 component of precipitation represents annual periodicity (c.12-13 months). For landform areas, the IMF2 components from the three rivers and three landform types typically had one main frequency, also with a period of around 12-months (Figure 10). Where the period of the IMF2 component is not 12 months, this reflects weak or absent seasonality in some years.

The decomposition shows that water and vegetated bar areas are close to being in phase with precipitation, with a lag of between 1 and 3 months. Unvegetated bar areas are close to anti-phase with precipitation, with peak areas always between March and May. Most sub-reaches of the three rivers show vegetation area expansion during September to December, with water surface area being maximum in August to November. Comparing the EEMD results with valley-scale geomorphology (Figure 6), there is no clear evidence that channel confinement controls annual changes in landform areas.

There are some periods of several months when the landform areas did not change significantly, even though precipitation followed the normal seasonal trend (Figure 10). In some cases, this reflects data gaps due to clouds obscuring the river in some images. For example, the Bislak River, reaches 2 and 3 (Figure 10, light grey shading) remained constant during 2017 due to data gaps, which also affected the Bislak River reach 5 in 2016.

Where data are available continuously, the EEMD analysis could potentially provide an approach to detect anthropogenic disturbance such as gravel mining. For example, in Abra River reach 2 in 2021, the water area maintained close to its peak value and the unvegetated bar area remained low (Figure 10, light grey shading), although the area of vegetated bars followed a typical seasonal pattern (light green shading). When we refer to the spectral imagery in Figure S13, the unvegetated bars area was occupied, an obvious artificial bank was changed (in red circle) and water area was extended (in blue circle) between 11 March 2020 and 11 March 2021. As well as bank construction, these changes may also be affected by gravel mining activities. If mining is important, changes may be expected in active width (AW) over succeeding years (Bertrand & Liebault, 2019).

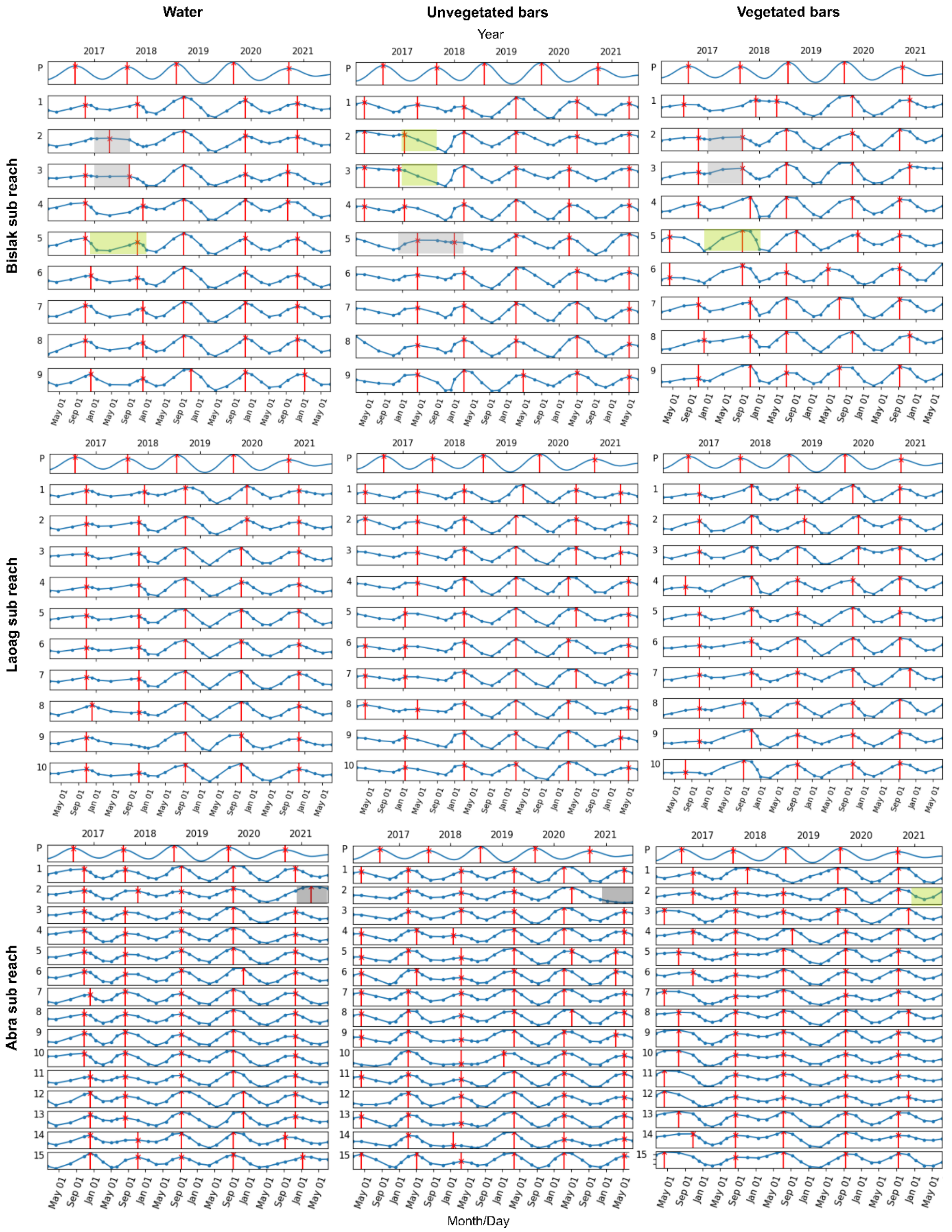

Figure 10. Ensemble Empirical Mode Decomposition (EEMD) IMF for precipitation (P; IMF 4) and landform (water, unvegetated bars, vegetated bars; IMF 2) areas. IMF 2 data (blue lines) are presented for sub-reaches (numbers as in Figure 6) for the Bislak, Laoag and Abra Rivers. In all cases, the periodicity is c.12-13 months. Red vertical lines are at each annual peak. Periods with light grey shading are not consistent with neighbouring reaches, whereas the light green shading shows periods that are consistent. See the text for explanations.

5. DISCUSSION

5.1 River pattern classification

A hierarchical workflow (Li et al., 2022) has been applied to three rivers intra-annually, using free-to-access remote sensing data. The workflow adopted object-based analysis, as recommended by previous land surface classification investigations (Demarchi et al., 2016; Ma et al., 2017; Phiri, Simwanda, & Nyirenda, 2021; Phiri et al., 2020). We applied the ATPRK algorithm to enhance the 20 m resolution Sentinel-2 imagery to 10 m resolution images. ATPRK was shown to be effective on Sentinel-2 imagery fusion by Q. M. Wang et al. (2016) and has been confirmed by Li et al. (2022) and our implementation here. However, we suggest it is essential to carefully choose and test downscaling approaches before applying object-based image classification. In addition to image downscaling, we also employed the LSMS algorithm, in open-source Orfeo-Toolbox, to perform an object-based segmentation. Ma et al. (2017) found that 80.9% of previous investigations have used commercial e-cognition software in their review of different software that has been applied to segment remote sensing imagery. Here, we obtained good classification results (overall above 0.86 in yearly overall accuracies for the three rivers) by using open-source software. Since Sentinel-2 is one of the most suitable satellite missions for monitoring vegetation with a medium to high spatial and temporal resolution, our investigation demonstrates the potential use of an open-source software workflow in fluvial settings.

Our classification results demonstrate that generating an active channel extent from multi-temporal data is useful for bounding the segmented geographical objects. This approach is especially important for the characterisation of tropical river dynamics as landforms within the active channel change more frequently than those in temperate settings due to the relatively high frequency of high flow events and strong seasonal effects. The latter have been described as the dominant feature of most tropical rivers (Syvitski et al., 2014). Due to the strong seasonality that is characteristic of the climate in north-west Luzon, we found that the single date-based machine learning model poorly fitted to imagery from a different season, whilst a multi-date based model was able to achieve higher accuracy across different dates of the year. From field observations, vegetation composition and condition vary seasonally, especially at the edges of the active channel due to agriculture development practices. For example, for a sub-reach of the Abra River (Figure S14) we identified agricultural activities on 11 January 2019, as patches of water disconnected from the main channel were observed. Looking at the same location over 5 years, we found the similar patterns between January and February in every year. This variation led us to consider a multi-season classification model for change detection in the studied rivers.

5.2 Spatial river landform sensitivity to channel settings

Whilst longer-term (>50 year) geomorphological processes, linked to tectonics, regional catchment settings and sediment supply, can cause changes in channel pattern (Baena-Escudero, Rinaldi, Garcia-Martinez, Guerrero-Amador, & Nardi, 2019; Corenblit et al., 2020; Gilvear, 1999), we constrained our study to a relatively short-term scale. In this section, we investigate landform stability, by establishing a covariance series of each landform area along each river, from downstream to upstream, for the 5.5-year time period. The coefficient of variation (COV) of a distribution is measured by the ratio of its standard deviation to its mean. This is designed to enable the comparison of series with different mean values. Large values of COV are associated with more dispersed distributions (X. J. Yang & Lo, 2000). We used a moving average window (9 data points) to smooth the COV series.

Figure 11 shows the longitudinal distribution of COV results, with confinement, faults and tributary locations indicated. Interpreted together with Figure 6, in general where faults are perpendicular to the channel centreline, vegetated bar stability increases. Conversely, where faults area at oblique angles to the channel centreline, vegetated bar stability decreases. Additionally, greater variability in the located of wetted areas is observed downstream of faults (for example, downstream of 11 km in the Abra River), which may reflect decreased gradient downstream of these faults. Where faults influence valley slope channel pattern adjusts, potentially leading to changes in sinuosity (Zámolyi, Székely, Draganits, & Timár, 2010), incision or the onset of wandering or braided behaviour. A sinuous reach downstream of the fault on the Bislak River at 27 km (Figure 6) indicates that the fault affects valley gradient and so causes increased meandering (Zámolyi, Székely, Draganits, & Timár, 2010).

Tributaries provide inputs of water and sediment that may impact mainstem morphology depending on the scale of these inputs and the calibre of introduced sediment (Ferguson & Hoey, 2008). In the Laoag River (Figure 11), the area occupied by water is highly unstable upstream of the three significant tributaries (ca. 33-40 km downstream; Figure 6, reach 7 and 8), whilst unvegetated bars remain stable and vegetated bar proportions are relatively low but showing seasonality (Figure 5) in this reach. In the meantime, Figure 6 shows that the water frequency is extremely low in this reach. In this case, downstream of tributaries the wetted channel becomes more stable. A similar result is observed for some tributaries in the Laoag and Abra Rivers where the wetter area becomes somewhat more stable downstream of tributary inputs. The impacts of tributaries depend on their sediment loads which we have not been able to quantify, and tributary locations are likely to be determined by fault locations and lithological changes. Hence, further investigation is required to understand the impacts of tributaries on channel form.

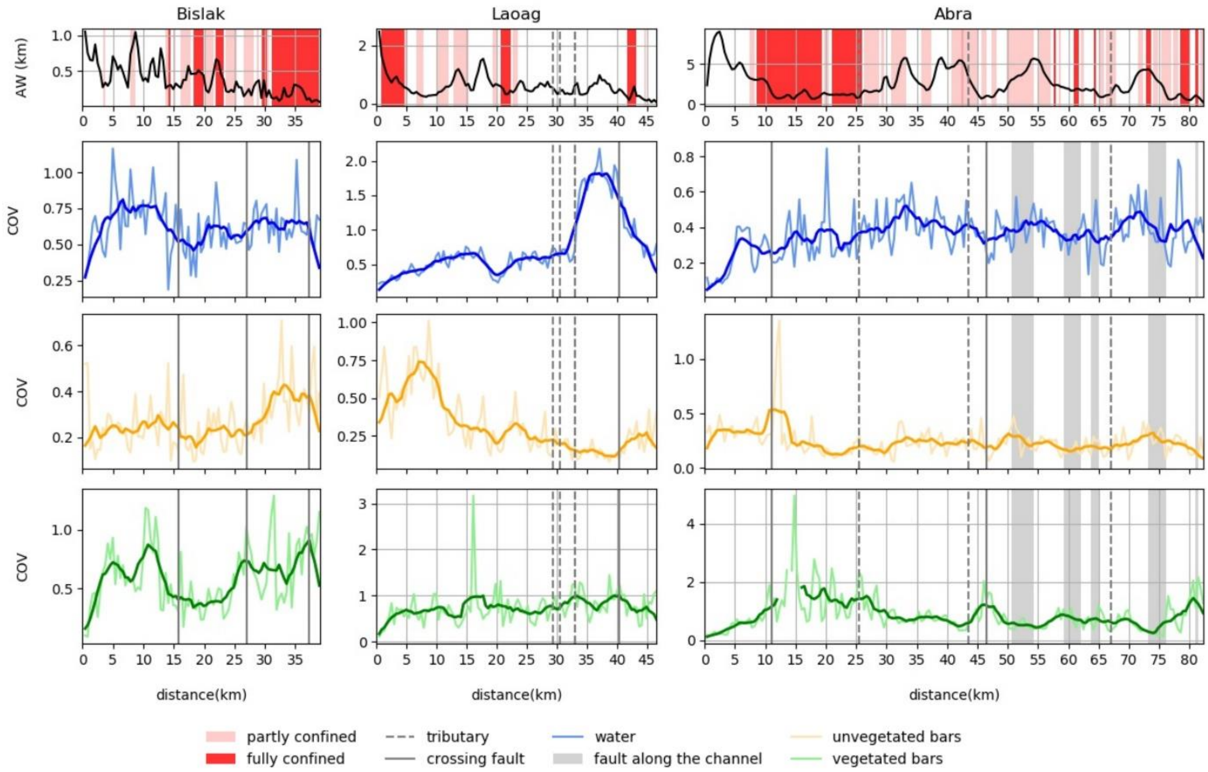

Figure 11. Channel settings, including active width, degree of confinement (confined / partly confined / unconfined), compared to the covariance (COV) spatial landform series for the Bislak, Laoag and Abra Rivers (water, unvegetated bars and vegetated bars shaded in thick lines are represented by smoothed values).

Fryirs (2017) reviewed challenges in analysing river sensitivity in geomorphology and argued that each river has its own history and ability to response to a give disturbance; this is also demonstrated in our investigation. Even though the three studied rivers are located near to each other and in the similar hydrological/climate system, the abilities they have to response to channel setting change are different. For example, in the Bislak River, unvegetated bars are extremely sensitive to continuous confined reach, whilst the unvegetated bars are also sensitive to partly confined reaches in the Laoag River. However, the unvegetated bars shows less sensitivity to the confinement in the Abra River. The Bislak River (0.0045 m/m) is significantly steeper than the Laoag (0.0029 m/m) and Abra (0.0018 m/m) Rivers, which may lead to higher sediment transport capacity in the Bislak. Moreover, averaged active width of the Abra River (2.626 km) is much wider than that of the Laoag (0.581 km) and Bislak (0.375 km) Rivers. In this study, steeper (i.e., those with higher sediment transport capacity) and narrower rivers tend to be more sensitive to lateral confinement. Transport capacity, sediment availability and lateral confinement interact to determine the locations of transport reaches and sedimentation zones (Church and Jones, 1983), and hence bar stability.

6. CONCLUSIONS

This investigation used a SVM machine learning method to classify tropical river landforms from multispectral, multi-temporal satellite imagery. Applied to three gravel-bed rivers in the Philippines, the machine learning method enabled rapid and objective classification of water, unvegetated bars and vegetated bars from Sentinel-2 imagery between 2016 and 2021. The overall accuracy (OA) exceeded 0.86 for all rivers, indicating that the model had an acceptable classification performance to analyse and interpret seasonal and annual changes in tropical river pattern.

Our results show longitudinal and temporal variation in landform areas and proportions (Figure 5). Longitudinal variation is strongly influenced by channel setting (e.g., active width, catchment size, confinement, tributaries and elevation). Landform areas are significantly correlated with active width (Figure 8 and 9), with the strongest correlation found between active width and vegetated bar area. Assessing longitudinal landform stability through the coefficient of variation (Figure 11), differences in gradient and the influence of faults demonstrated how rivers in similar hydrological/climate regimes can have different river sensitivities. Temporally, we show synchronous changes in the area/proportion of landform units between rivers. During the dry season, increases in the proportion of water corresponds to significant decreases in the proportion of unvegetated bars in the Bislak and Abra Rivers, whilst the relationship applies to both the wet and dry seasons of the Laoag River. The finding suggests the need to consider tropical river pattern as a dynamic entity; characterising river pattern from a single time period may not fully represent the considerable impact of seasonal change.

Temporal patterns in landform areas across sub-reaches of each river were assessed using Ensemble Empirical Mode Decomposition (EEMD) to decompose time series of classified water, unvegetated bar and vegetated bar areas (Figure 10). For landform areas, the IMF2 components from the three rivers and three landform types typically had one main frequency with a period of around 12-months. The data suggest water and vegetated bars commonly have a synchronised fluctuation with precipitation (close to in-phase), while unvegetated bars have an oscillation close to anti-phase with precipitation. The peak area of water and vegetated bars have a 1 to 3 months lag from the peak of precipitation in each year, while the peak for unvegetated bars occurred between March and May of every year. The time series decomposition method has capacity to detect local (sub-reach) abrupt change through consistency of the decomposed signal; deviations from periodic consistency in river pattern may reflect the influence of extreme events and/or human disturbance. We recommend EEMD as an appropriate statistical technique in geomorphology to decompose datasets that are generated from contemporary applications of machine learning to remotely sensed imagery.

REFERENCES

Abanco, C., Bennett, G. L., Matthews, A. J., Matera, M. A. M., & Tan, F. J. (2021). The role of geomorphology, rainfall and soil moisture in the occurrence of landslides triggered by 2018 Typhoon Mangkhut in the Philippines. Natural Hazards and Earth System Sciences, 21(5), 1531-1550. doi:10.5194/nhess-21-1531-2021

Abon, C. C., David, C. P. C., & Pellejera, N. E. B. (2011). Reconstructing the Tropical Storm Ketsana flood event in Marikina River, Philippines. Hydrology and Earth System Sciences, 15(4), 1283-1289. doi:10.5194/hess-15-1283-2011

Baena-Escudero, R., Rinaldi, M., Garcia-Martinez, B., Guerrero-Amador, I. C., & Nardi, L. (2019). Channel adjustments in the lower Guadalquivir River (southern Spain) over the last 250 years. Geomorphology, 337, 15-30. doi:10.1016/j.geomorph.2019.03.027

Bagtasa, G. (2017). Contribution of Tropical Cyclones to Rainfall in the Philippines. Journal of Climate, 30(10), 3621-3633. doi:10.1175/Jcli-D-16-0150.1

Bertrand, M., & Liebault, F. (2019). Active channel width as a proxy of sediment supply from mining sites in New Caledonia. Earth Surface Processes and Landforms, 44(1), 67-76. doi:10.1002/esp.4478

Boothroyd, R. J., Williams, R. D., Hoey, T. B., Barrett, B., & Prasojo, O. A. (2021). Applications of Google Earth Engine in fluvial geomorphology for detecting river channel change. Wiley Interdisciplinary Reviews-Water, 8(1). doi:10.1002/wat2.1496

Buffington, J. M., & Montgomery, D. R. (2022). Geomorphic Classification of Rivers: An Updated Review. In Treatise on Geomorphology (pp. 1143-1190).

Carlson, T. N., & Ripley, D. A. (1997). On the relation between NDVI, fractional vegetation cover, and leaf area index. Remote Sensing of Environment, 62(3), 241-252. doi:10.1016/S0034-4257(97)00104-1

Cerna, M., & Harvey, A. F. (2000). The fundamentals of FFT-based signal analysis and measurement. Retrieved from
Church, M. (2006). Bed Material Transport and the Morphology of Alluvial River Channels. Annual Review of Earth and Planetary Sciences, 34(1), 325-354. doi:10.1146/annurev.earth.33.092203.122721

Cinco, T. A., de Guzman, R. G., Ortiz, A. M. D., Delfino, R. J. P., Lasco, R. D., Hilario, F. D., . . . Ares, E. D. (2016). Observed trends and impacts of tropical cyclones in the Philippines. International Journal of Climatology, 36(14), 4638-4650. doi:10.1002/joc.4659

Comaniciu, D., & Meer, P. (2002). Mean shift: A robust approach toward feature space analysis. Ieee Transactions on Pattern Analysis and Machine Intelligence, 24(5), 603-619. doi:10.1109/34.1000236

Corenblit, D., Vautier, F., Gonzalez, E., & Steiger, J. (2020). Formation and dynamics of vegetated fluvial landforms follow the biogeomorphological succession model in a channelized river. Earth Surface Processes and Landforms, 45(9), 2020-2035. doi:10.1002/esp.4863

De Luca, G., Silva, J. M. N., Cerasoli, S., Araujo, J., Campos, J., Di Fazio, S., & Modica, G. (2019). Object-Based Land Cover Classification of Cork Oak Woodlands using UAV Imagery and Orfeo ToolBox. Remote Sensing, 11(10). doi:10.3390/rs11101238

Demarchi, L., Bizzi, S., & Piegay, H. (2016). Hierarchical Object-Based Mapping of Riverscape Units and in-Stream Mesohabitats Using LiDAR and VHR Imagery. Remote Sensing, 8(2). doi:10.3390/rs8020097

Demarchi, L., Bizzi, S., & Piegay, H. (2017). Regional hydromorphological characterization with continuous and automated remote sensing analysis based on VHR imagery and low-resolution LiDAR data. Earth Surface Processes and Landforms, 42(3), 531-551. doi:10.1002/esp.4092

Dingle, E. H., Paringit, E. C., Tolentino, P. L. M., Williams, R. D., Hoey, T. B., Barrett, B., . . . Stott, E. (2019). Decadal-scale morphological adjustment of a lowland tropical river. Geomorphology, 333, 30-42. doi:10.1016/j.geomorph.2019.01.022

Ferguson, R., & Hoey, T. (2008). Effects of Tributaries on Main-Channel Geomorphology. In River Confluences, Tributaries and the Fluvial Network (pp. 183-208).

Fryirs, K. A. (2017). River sensitivity: a lost foundation concept in fluvial geomorphology. Earth Surface Processes and Landforms, 42(1), 55-70. doi:10.1002/esp.3940

Gao, B. C. (1996). NDWI - A normalized difference water index for remote sensing of vegetation liquid water from space. Remote Sensing of Environment, 58(3), 257-266. doi:10.1016/S0034-4257(96)00067-3

Gilvear, D. J. (1999). Fluvial geomorphology and river engineering: future roles utilizing a fluvial hydrosystems framework. Geomorphology, 31(1-4), 229-245. doi:10.1016/S0169-555x(99)00086-0

Grafil, L., & Castro, O. (2014). Acquisition of IfSAR for the production of nationwide DEM and ORI for the Philippines under the unified mapping project. Infomapper, 21(12-13), 40-43.

Gran, K. B., & Montgomery, D. R. (2005). Spatial and temporal patterns in fluvial recovery following volcanic eruptions: Channel response to basin-wide sediment loading at Mount Pinatubo, Philippines. Geological Society of America Bulletin, 117(1-2), 195-211. doi:10.1130/B25528.1

Gurnell, A. M., Rinaldi, M., Belletti, B., Bizzi, S., Blamauer, B., Braca, G., . . . Ziliani, L. (2016). A multi-scale hierarchical framework for developing understanding of river behaviour to support river management. Aquatic Sciences, 78(1), 1-16. doi:10.1007/s00027-015-0424-5

Hajdukiewicz, H., & Wyzga, B. (2019). Aerial photo-based analysis of the hydromorphological changes of a mountain river over the last six decades: The Czarny Dunajec, Polish Carpathians. Science of the Total Environment, 648, 1598-1613. doi:10.1016/j.scitotenv.2018.08.234

Ham, D., & Church, M. (2012). Morphodynamics of an extended bar complex, Fraser River, British Columbia. Earth Surface Processes and Landforms, 37(10), 1074-1089. doi:10.1002/esp.3231

Holden, D., Saito, J., & Komura, T. (2016). A Deep Learning Framework for Character Motion Synthesis and Editing. Acm Transactions on Graphics, 35(4). doi:10.1145/2897824.2925975

Hooke, J. M. (2022). Morphodynamics of a meandering channel over decadal timescales in response to hydrological variations. Earth Surface Processes and Landforms, 47(8), 1902-1920. doi:10.1002/esp.5354

Horacio, J., Ollero, A., & Perez-Alberti, A. (2017). Geomorphic classification of rivers: a new methodology applied in an Atlantic Region (Galicia, NW Iberian Peninsula). Environmental Earth Sciences, 76(21). doi:10.1007/s12665-017-7072-0

Huang, N. E., Shen, Z., Long, S. R., Wu, M. L. C., Shih, H. H., Zheng, Q. N., . . . Liu, H. H. (1998). The empirical mode decomposition and the Hilbert spectrum for nonlinear and non-stationary time series analysis. Proceedings of the Royal Society a-Mathematical Physical and Engineering Sciences, 454(1971), 903-995. doi:10.1098/rspa.1998.0193

Huang, Z. W. N. E. (2004). A study of the characteristics of white noise using the empirical mode decomposition method. The Royal Society, 1597-1611.

Huete, A., Didan, K., Miura, T., Rodriguez, E. P., Gao, X., & Ferreira, L. G. (2002). Overview of the radiometric and biophysical performance of the MODIS vegetation indices. Remote Sensing of Environment, 83(1-2), 195-213. doi:10.1016/S0034-4257(02)00096-2

Huete, A. R. (1988). A Soil-Adjusted Vegetation Index (Savi). Remote Sensing of Environment, 25(3), 295-309. doi:10.1016/00344257(88)90106-X

Huffman, G.J., E.F. Stocker, D.T. Bolvin, E.J. Nelkin, Jackson Tan (2019), GPM IMERG Final Precipitation L3 Half Hourly 0.1 degree x 0.1 degree V06, Greenbelt, MD, Goddard Earth Sciences Data and Information Services Center (GES DISC). doi: 10.5067/GPM/IMERG/3B-HH/06

Ji, L., Zhang, L., Wylie, B. K., & Rover, J. (2011). On the terminology of the spectral vegetation index (NIR - SWIR)/(NIR + SWIR). International Journal of Remote Sensing, 32(21), 6901-6909. doi:10.1080/01431161.2010.510811

Jiang, Z. Y., Huete, A. R., Didan, K., & Miura, T. (2008). Development of a two-band enhanced vegetation index without a blue band. Remote Sensing of Environment, 112(10), 3833-3845. doi:10.1016/j.rse.2008.06.006

Jordan, M. I., & Mitchell, T. M. (2015). Machine learning: Trends, perspectives, and prospects. Science, 349(6245), 255-260. doi:10.1126/science.aaa8415

Kim, C. R. (2019). Framework of Extreme Flood Risk Management in the Typhoon Country Region. Tropical Cyclone Research and Review, 8(1), 35-45. doi:10.6057/2019tcrr01.01

Kondolf, G. M., Piégay, H., Schmitt, L., & Montgomery, D. R. (2016). Geomorphic classification of rivers and streams. In Tools in Fluvial Geomorphology (pp. 133-158).

Kong, Y. L., Meng, Y., Li, W., Yue, A. Z., & Yuan, Y. (2015). Satellite Image Time Series Decomposition Based on EEMD. Remote Sensing, 7(11), 15583-15604. doi:10.3390/rs71115583

Korhonen, L., Hadi, Packalen, P., & Rautiainen, M. (2017). Comparison of Sentinel-2 and Landsat 8 in the estimation of boreal forest canopy cover and leaf area index. Remote Sensing of Environment, 195, 259-274. doi:10.1016/j.rse.2017.03.021

Kubota, H., Shirooka, R., Matsumoto, J., Cayanan, E. O., & Hilario, F. D. (2017). Tropical cyclone influence on the long-term variability of

Philippine summer monsoon onset. Progress in Earth and Planetary Science, 4. doi:10.1186/s40645-017-0138-5

Laszuk D. 2017. PyEMD: Python implementation of Empirical Mode Decompoisition (EMD) method. Available: https://github.com/laszukdawid/PyEMD.

Li, Q., Barrett, B., Williams, R., Hoey, T., & Boothroyd, R. (2022). Enhancing performance of multi-temporal tropical river landform classification through downscaling approaches. International Journal of Remote Sensing, 43(17), 6445-6462. doi:10.1080/01431161.2022.2139164

Liu, Z. F., Zhao, Y. L., Colin, C., Siringan, F. P., & Wu, Q. (2009). Chemical weathering in Luzon, Philippines from clay mineralogy and major-element geochemistry of river sediments. Applied Geochemistry, 24(11), 2195-2205. doi:10.1016/j.apgeochem.2009.09.025

Ma, L., Li, M. C., Ma, X. X., Cheng, L., Du, P. J., & Liu, Y. X. (2017). A review of supervised object-based land-cover image classification. Isprs Journal of Photogrammetry and Remote Sensing, 130, 277-293. doi:10.1016/j.isprsjprs.2017.06.001

Main-Knorn, M., Pflug, B., Louis, J., Debaecker, V., Muller-Wilm, U., & Gascon, F. (2017). Sen2Cor for Sentinel-2. Image and Signal Processing for Remote Sensing Xxiii, 10427. doi:10.1117/12.2278218

Mandarino, A., Maerker, M., & Firpo, M. (2019). Channel planform changes along the Scrivia River floodplain reach in northwest Italy from 1878 to 2016. Quaternary Research, 91(2), 620-637. doi:10.1017/qua.2018.67

Maxwell, K. V., Ramos, N. T., Tsutsumi, H., Chou, Y. C., Duan, F., & Shen, C. C. (2018). Late Quaternary uplift across northwest Luzon Island, Philippines constrained from emergent coral reef terraces. Earth Surface Processes and Landforms, 43(15), 3114-3132. doi:10.1002/esp.4474

Ming, D. P., Yang, J. Y., Li, L. X., & Song, Z. Q. (2011). Modified ALV for selecting the optimal spatial resolution and its scale effect on image classification accuracy. Mathematical and Computer Modelling, 54(3-4), 1061-1068. doi:10.1016/j.mcm.2010.11.036

Mohguen, W., & Bekka, R. E. (2015). Improvement of Ensemble Empirical Mode Decomposition by a Band-Limited White Noise. 2015 4th International Conference on Electrical Engineering (Icee), 397-+.

Ohsaki, M., Wang, P., Matsuda, K., Katagiri, S., Watanabe, H., & Ralescu, A. (2017). Confusion-Matrix-Based Kernel Logistic Regression for Imbalanced Data Classification. Ieee Transactions on Knowledge and Data Engineering, 29(9), 1806-1819. doi:10.1109/Tkde.2017.2682249

Paola, C. (2017). A Mind of Their Own: Recent Advances in Autogenic Dynamics in Rivers and Deltas. In Autogenic Dynamics and Self-Organization in Sedimentary Systems (pp. 5-17).

Philippine Institute of Volcanology and Seismology (PHIVOLCS) (2015) Distribution of active faults and trenches in the Philippines map. https://www.phivolcs.dost.gov.ph/index.php/earthquake/earthquake-generators-of-the-philippines. Accessed 20 July 2021

Phiri, D., Simwanda, M., & Nyirenda, V. (2021). Mapping the impacts of cyclone Idai in Mozambique using Sentinel-2 and OBIA approach. South African Geographical Journal, 103(2), 237-258. doi:10.1080/03736245.2020.1740104

Phiri, D., Simwanda, M., Salekin, S., Nyirenda, V. R., Murayama, Y., & Ranagalage, M. (2020). Sentinel-2 Data for Land Cover/Use Mapping: A Review. Remote Sensing, 12(14). doi:10.3390/rs12142291

Prakash, N., Manconi, A., & Loew, S. (2020). Mapping Landslides on EO Data: Performance of Deep Learning Models vs. Traditional Machine Learning Models. Remote Sensing, 12(3). doi:10.3390/rs12030346

Rabanaque, M. P., Martinez-Fernandez, V., Calle, M., & Benito, G. (2022). Basin-wide hydromorphological analysis of ephemeral streams using machine learning algorithms. Earth Surface Processes and Landforms, 47(1), 328-344. doi:10.1002/esp.5250

Reid, H. E., & Brierley, G. J. (2015). Assessing geomorphic sensitivity in relation to river capacity for adjustment. Geomorphology, 251, 108-121. doi:10.1016/j.geomorph.2015.09.009

Ridder, D. (2011). Comparison between eemd, wavelet and fir denoising: Influence on event detection in impedance cardiography.

Rodrigues, M. O., Abrantes, N., Goncalves, F. J. M., Nogueira, H., Marques, J. C., & Goncalves, A. M. M. (2018). Spatial and temporal distribution of microplastics in water and sediments of a freshwater system (Antua River, Portugal). Science of the Total Environment, 633, 1549-1559. doi:10.1016/j.scitotenv.2018.03.233

Saleem, A., Dewan, A., Rahman, M. M., Nawfee, S. M., Karim, R., & Lu, X. X. (2020). Spatial and Temporal Variations of Erosion and Accretion: A

Case of a Large Tropical River. Earth Systems and Environment, 4(1), 167-181. doi:10.1007/s41748-019-00143-8

Schneider, W. F., & Guo, H. (2018). Machine Learning. Journal of Physical Chemistry C, 122(4), 1889-1889. doi:10.1021/acs.jpcc.8b00036

Serlet, A. J., Gurnell, A. M., Zolezzi, G., Wharton, G., Belleudy, P., & Jourdain, C. (2018). Biomorphodynamics of alternate bars in a channelized, regulated river: An integrated historical and modelling analysis. Earth Surface Processes and Landforms, 43(9), 1739-1756. doi:10.1002/esp.4349

Sonobe, R., Yamaya, Y., Tani, H., Wang, X. F., Kobayashi, N., & Mochizuki, K. (2018). Crop classification from Sentinel-2-derived vegetation indices using ensemble learning. Journal of Applied Remote Sensing, 12(2). doi:10.1117/1.Jrs.12.026019

Spada, D., Molinari, P., Bertoldi, W., Vitti, A., & Zolezzi, G. (2018). Multi-Temporal Image Analysis for Fluvial Morphological Characterization with Application to Albanian Rivers. Isprs International Journal of Geo-Information, 7(8). doi:10.3390/ijgi7080314

Syvitski, J. P. M., Cohen, S., Kettner, A. J., & Brakenridge, G. R. (2014). How important and different are tropical rivers? - An overview. Geomorphology, 227, 5-17. doi:10.1016/j.geomorph.2014.02.029

Tolentino, P. L. M., Perez, J. E. G., Guardian, E. L., Boothroyd, R. J., Hoey, T. B., Williams, R. D., . . . David, C. P. C. (2022). River Styles and stream power analysis reveal the diversity of fluvial morphology in a Philippine tropical catchment. Geoscience Letters, 9(1). doi:10.1186/s40562-022-00211-4

Torres, M. E., Colominas, M. A., Schlotthauer, G., & Flandrin, P. (2011). A Complete Ensemble Empirical Mode Decomposition with Adaptive Noise. 2011 Ieee International Conference on Acoustics, Speech, and Signal Processing, 4144-4147.

Veloria, A., Perez, G. J., Tapang, G., & Comiso, J. (2021). Improved Rainfall Data in the Philippines through Concurrent Use of GPM IMERG and Ground-Based Measurements. Remote Sensing, 13(15), 2859. doi:10.3390/rs13152859

Wang, C., & Zhang, H. (2020). Trend and Variance of Continental Fresh Water Discharge over the Last Six Decades. Water, 12(12). doi:10.3390/w12123556

Wang, Q. M., Shi, W. Z., Li, Z. B., & Atkinson, P. M. (2016). Fusion of Sentinel-2 images. Remote Sensing of Environment, 187, 241-252. doi:10.1016/j.rse.2016.10.030

Wilson, E. H., & Sader, S. A. (2002). Detection of forest harvest type using multiple dates of Landsat TM imagery. Remote Sensing of Environment, 80(3), 385-396. doi:10.1016/S0034-4257(01)00318-2

Xu, X. J., Liu, H. Y., Lin, Z. S., Jiao, F. S., & Gong, H. B. (2019). Relationship of Abrupt Vegetation Change to Climate Change and Ecological Engineering with Multi-Timescale Analysis in the Karst Region, Southwest China. Remote Sensing, 11(13). doi:10.3390/rs11131564

Yang, X. C., Zhao, S. S., Qin, X. B., Zhao, N., & Liang, L. G. (2017). Mapping of Urban Surface Water Bodies from Sentinel-2 MSI Imagery at 10 m Resolution via NDWI-Based Image Sharpening. Remote Sensing, 9(6). doi:10.3390/rs9060596

Yang, X. J., & Lo, C. P. (2000). Relative radiometric normalization performance for change detection from multi-date satellite images. Photogrammetric Engineering and Remote Sensing, 66(8), 967-980.

Zámolyi, A., Székely, B., Draganits, E., & Timár, G. (2010). Neotectonic control on river sinuosity at the western margin of the Little Hungarian Plain. Geomorphology, 122(3-4), 231-243. doi:10.1016/j.geomorph.2009.06.028

SEASONAL AND ANNUAL TROPICAL RIVER PATTERN CHANGE DETECTION USING MACHINE LEARNING

Supplementary Figures

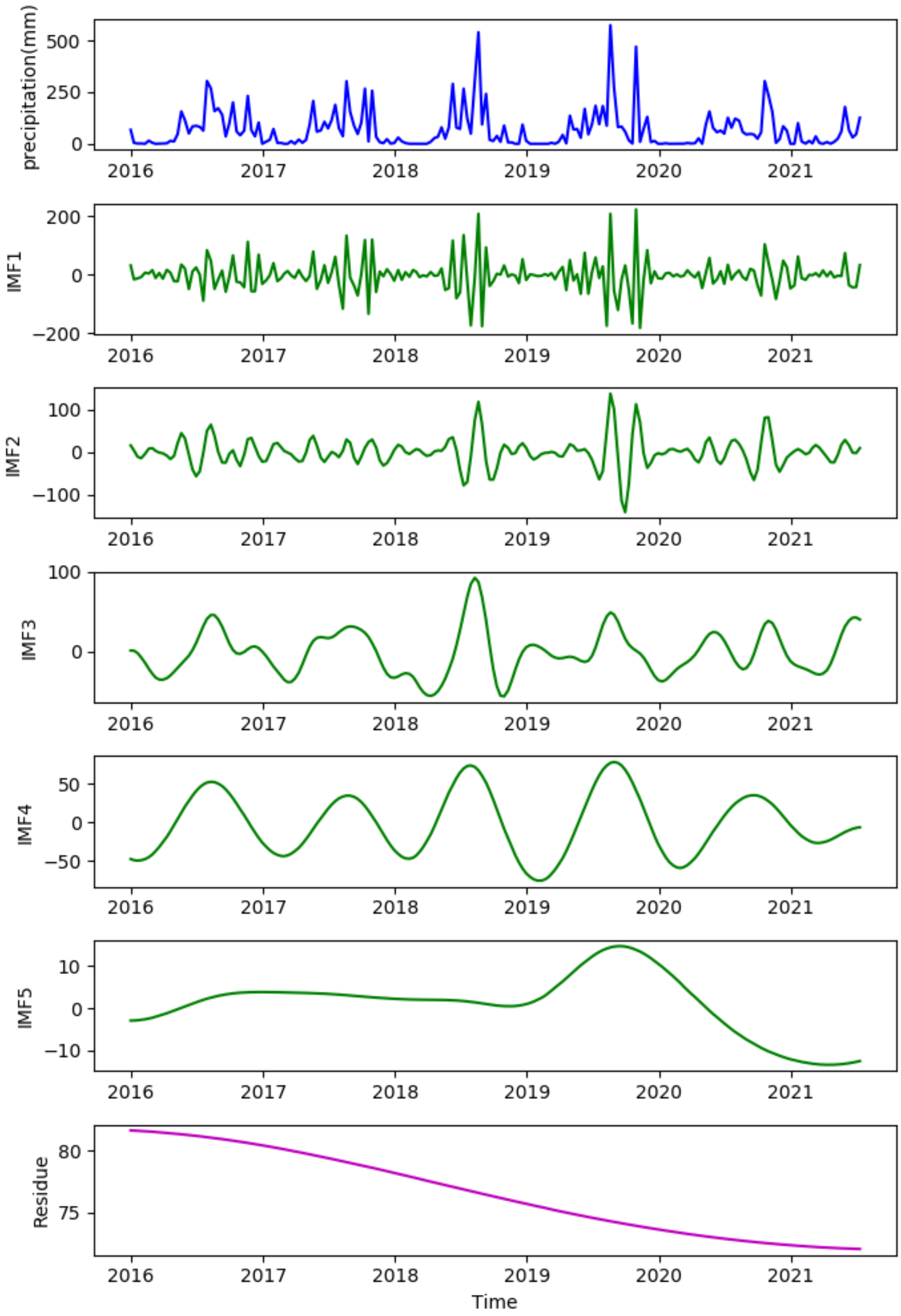

Figure S1. Ensemble Empirical Mode Decomposition (EEMD) on GPM IMERG catchment-averaged (every 10 days) precipitation data from the Bislak catchment. Upper plot (blue) is the precipitation data for the Bislak River catchment. The subsequent five plots (green) are decomposed Instinct Mode Functions (IMFs), and the lowest plot (purple) is the residual of the decomposition.

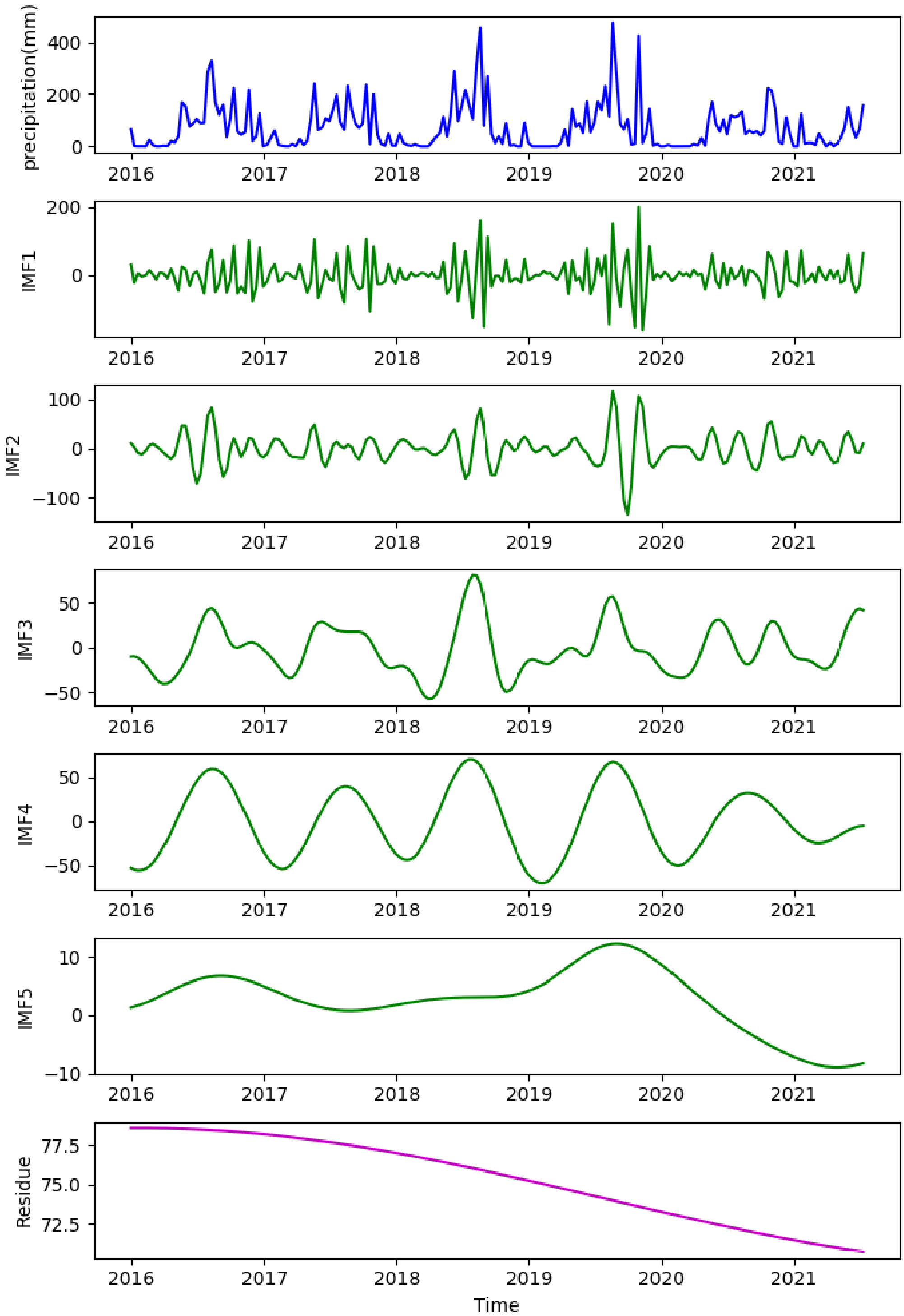

Figure S2. Ensemble Empirical Mode Decomposition (EEMD) on GPM IMERG catchment-averaged (every 10 days) precipitation data from the Laoag catchment. Upper plot (blue) is the precipitation data for the Laoag River catchment. The subsequent five plots (green) are decomposed Instinct Mode Functions (IMFs), and the lowest plot (purple) is the residual of the decomposition.

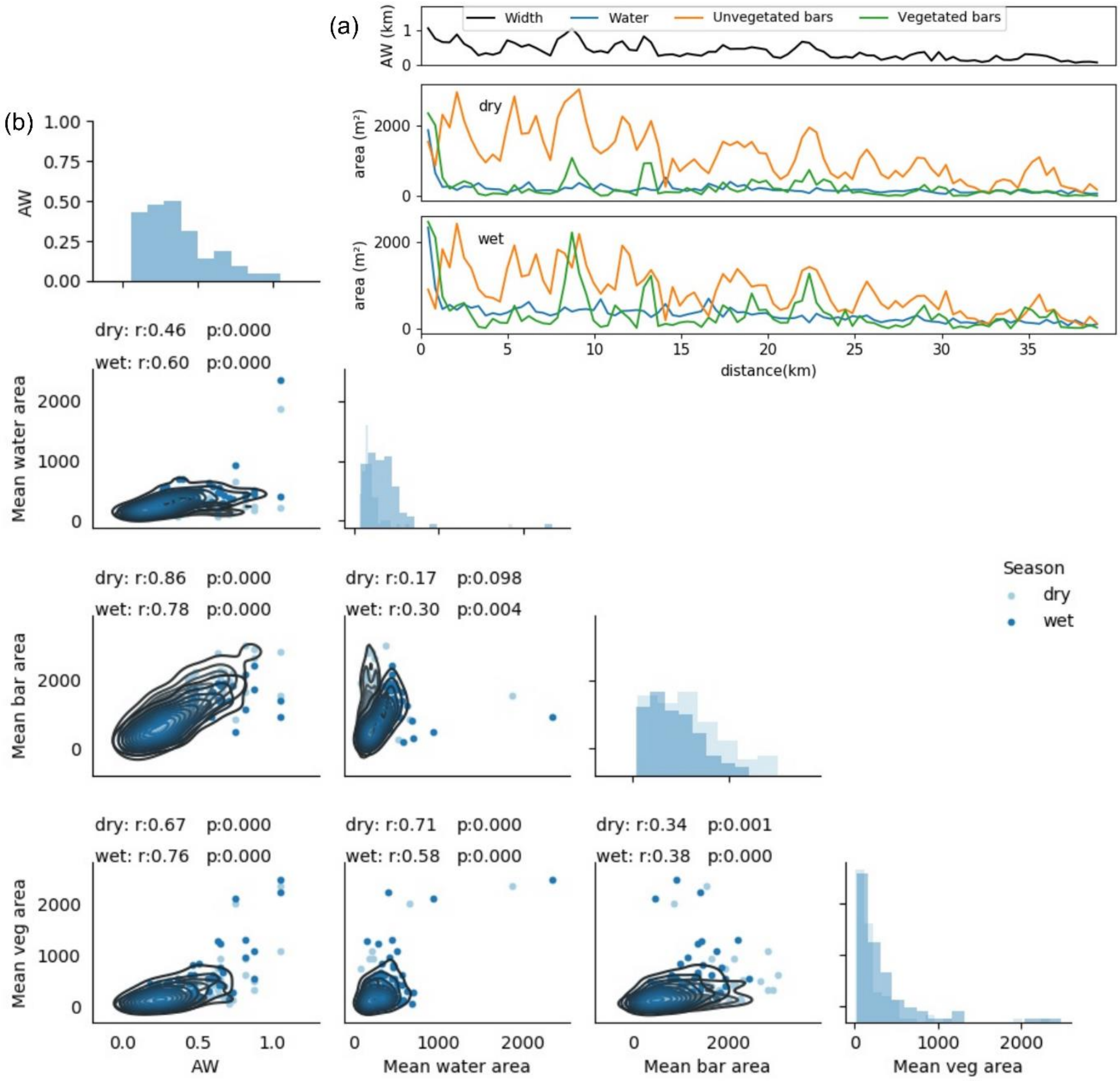

Figure S3. (a) Longitudinal trend in active width (AW) and mean area of three landforms (water, unvegetated bars, vegetated bars) for the Laoag River, for wet and dry seasons. (b) Matrix plots to represent correlations between mean values of landform areas and AW. Histograms illustrate mean value distributions at equal spaced spatial distance along the river. Kernel distribution estimation is shown using contour plots. Tables above each matrix plot summarise correlation coefficients (r) and associated statistical significance (p) between landforms area and AW in wet season and dry season.

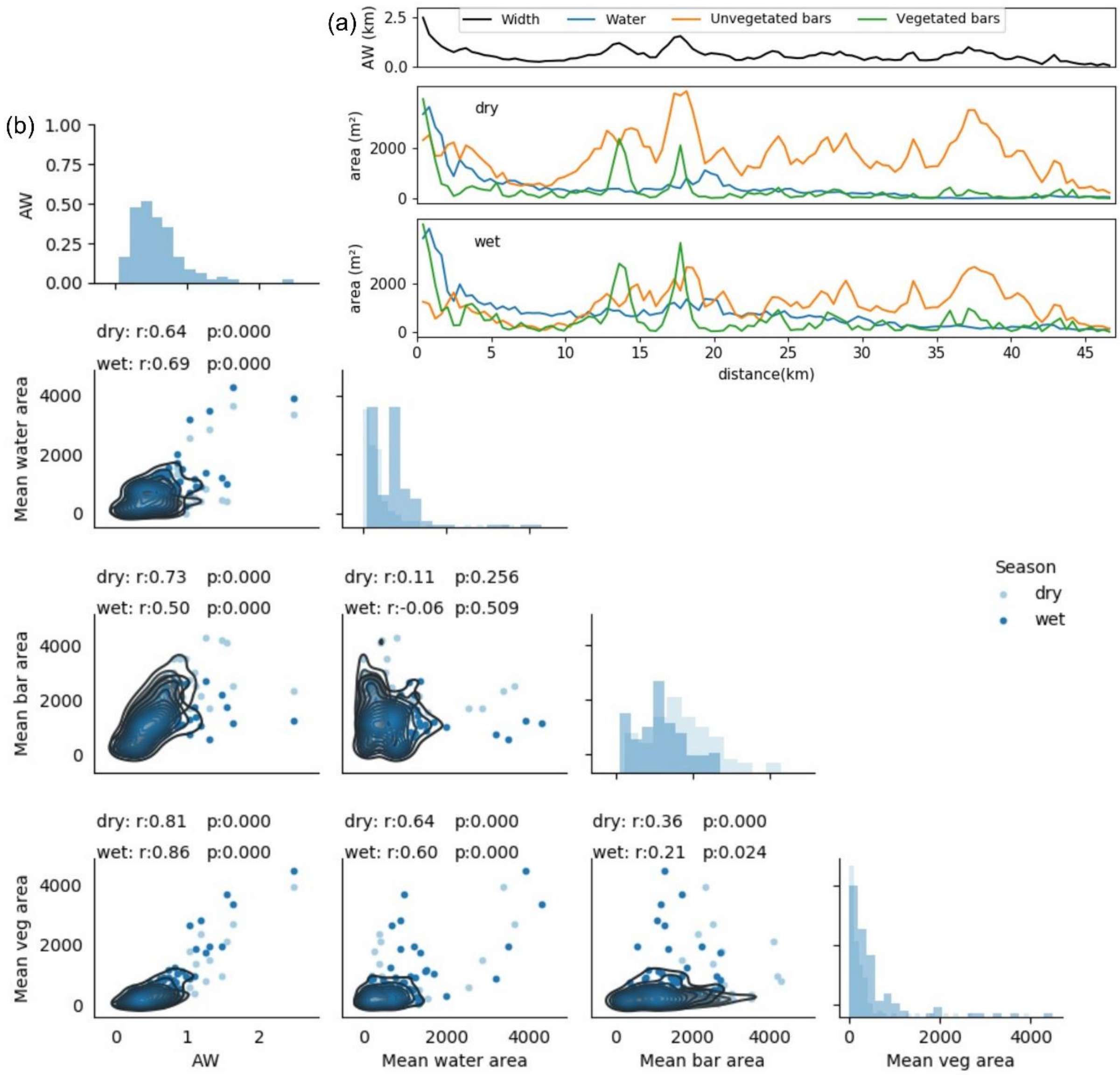

Figure S4. (a) Longitudinal trend in active width (AW) and mean area of three landforms (water, unvegetated bars, vegetated bars) for the Laoag River, for wet and dry seasons. (b) Matrix plots to represent correlations between mean values of landform areas and AW. Histograms illustrate mean value distributions at equal spaced spatial distance along the river. Kernel distribution estimation is shown using contour plots. Tables above each matrix plot summarise correlation coefficients (r) and associated statistical significance (p) between landforms area and AW in wet season and dry season.

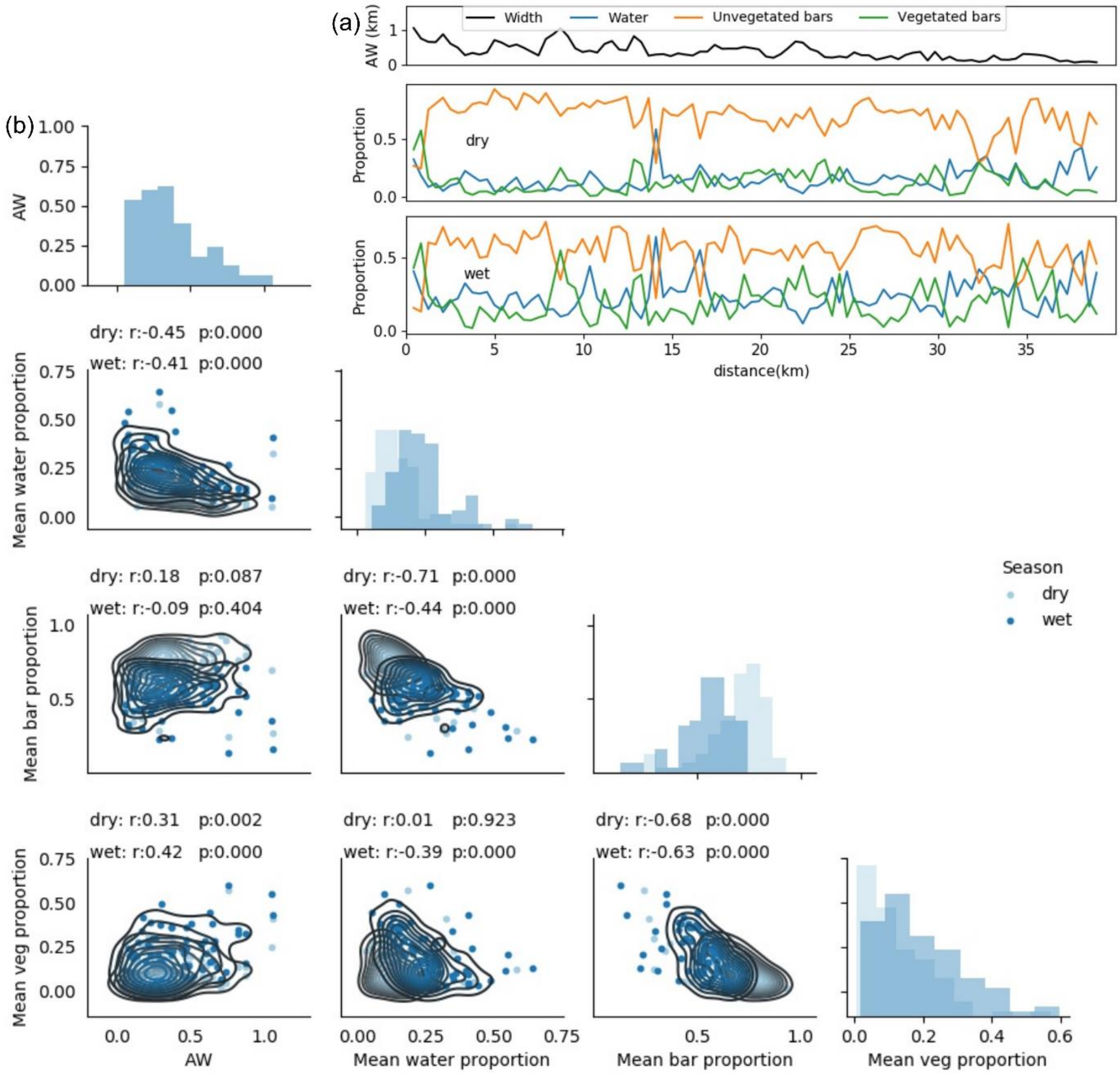

Figure S5. (a) Longitudinal trend in active width (AW) and mean proportion of three landforms (water, unvegetated bars, vegetated bars) for the Bislak River, for wet and dry seasons. (b) Matrix plots to represent correlations between mean values of landform proportions and AW. Histograms illustrate mean value distributions at ~410 m spatial distance along the river. Kernel distribution estimation is shown using contour plots. Tables above each matrix plot summarise correlation coefficients (r) and associated statistical significance (p) between landforms proportion and AW in wet season and dry season.

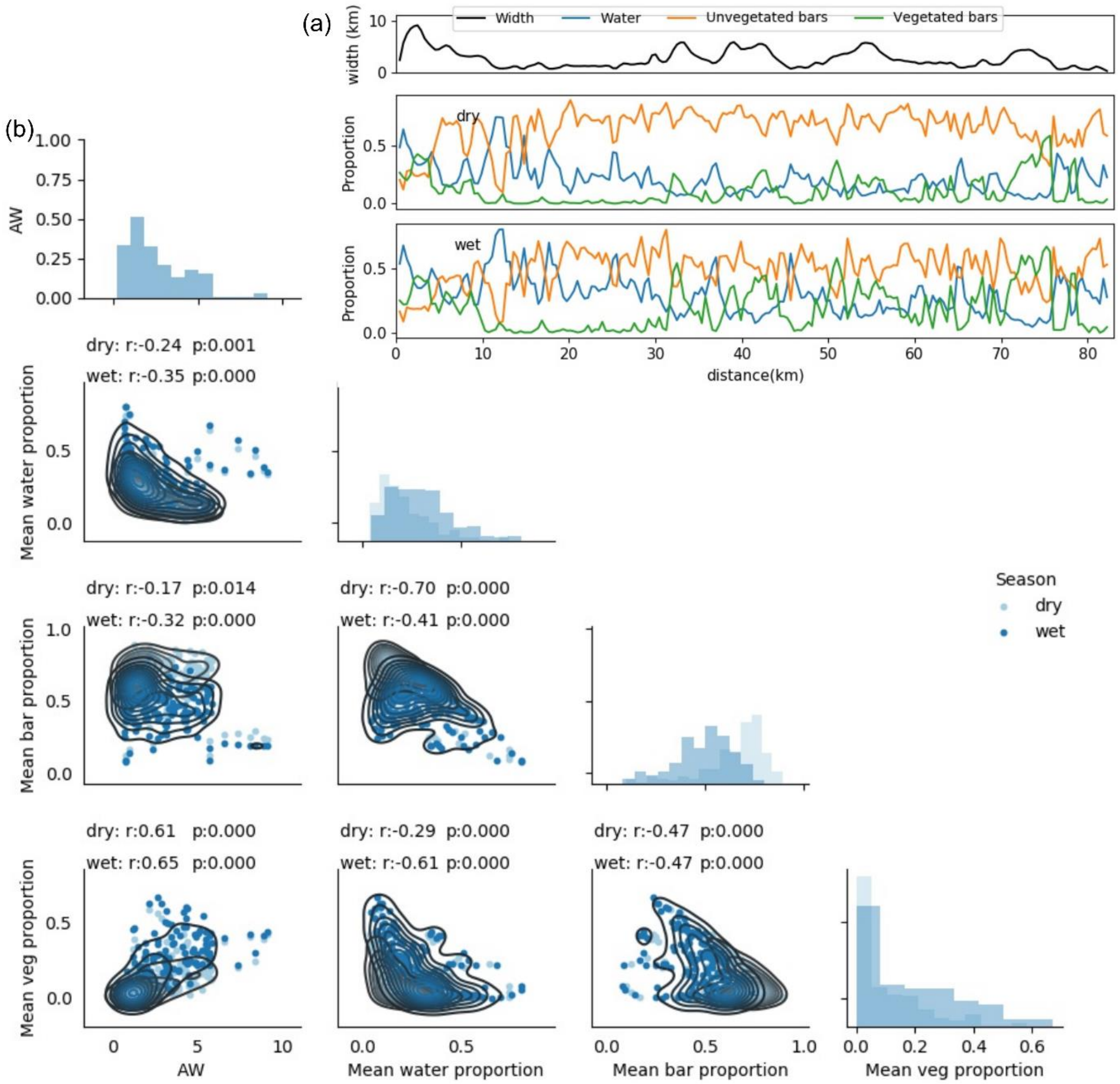

Figure S6. (a) Longitudinal trend in active width (AW) and mean proportion of three landforms (water, unvegetated bars, vegetated bars) for the Abra River, for wet and dry seasons. (b) Matrix plots to represent correlations between mean values of landform proportions and AW. Histograms illustrate mean value distributions at ~410 m spatial distance along the river. Kernel distribution estimation is shown using contour plots. Tables above each matrix plot summarise correlation coefficients (r) and associated statistical significance (p) between landforms proportion and AW in wet season and dry season.

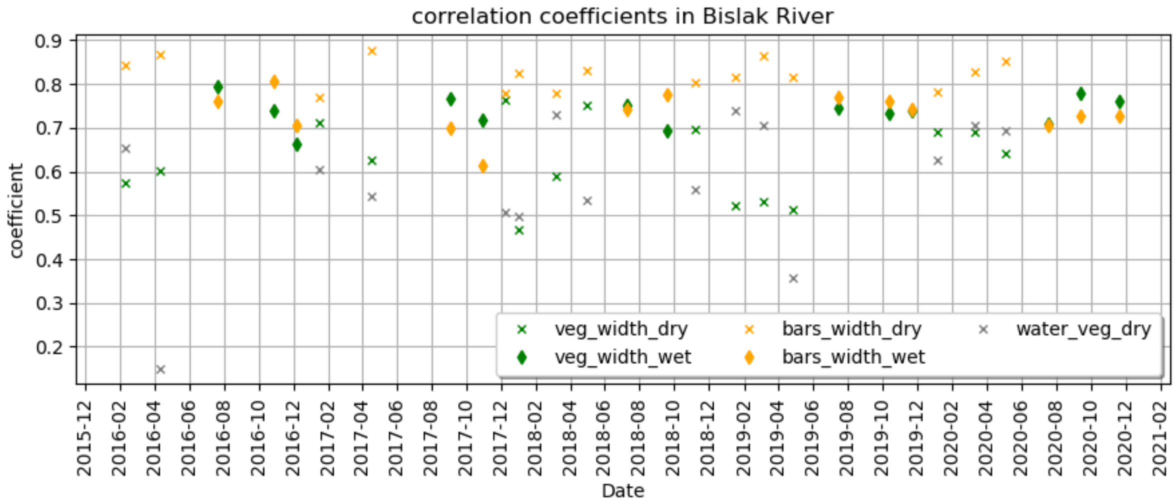

Figure S7. Bislak River landforms' area - AW correlation coefficients time series.

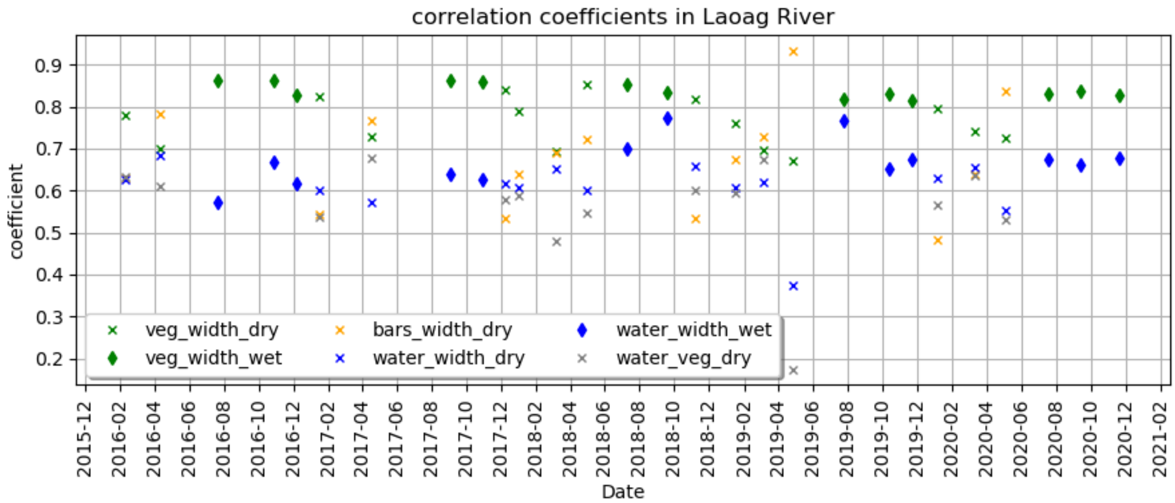

Figure S8. Laoag River landforms' area - AW correlation coefficients time series.

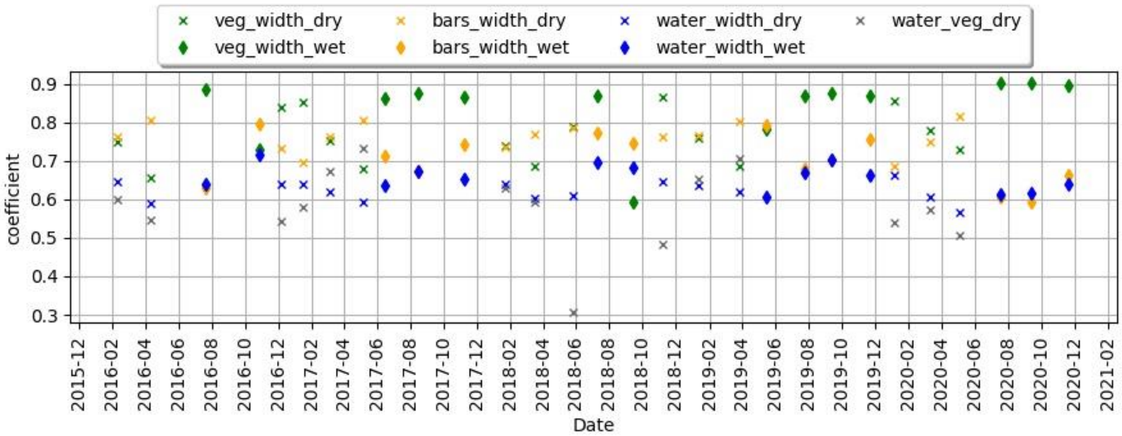

Figure S9. Abra River landforms’ area- AW correlation coefficients time series.

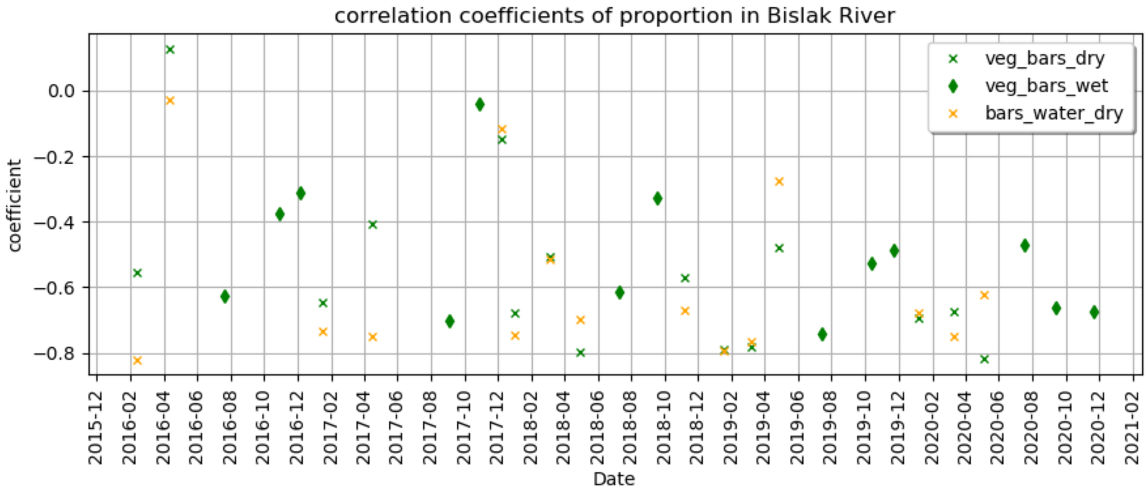

Figure S10. Bislak River landforms’ proportion- AW correlation coefficients time series.

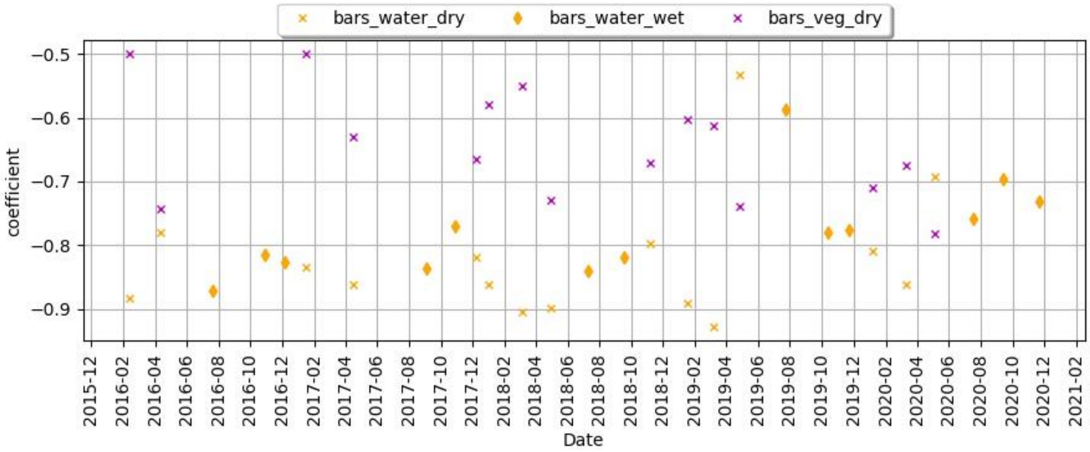

Figure S11. Laoag River landforms' proportion- AW correlation coefficients time series.

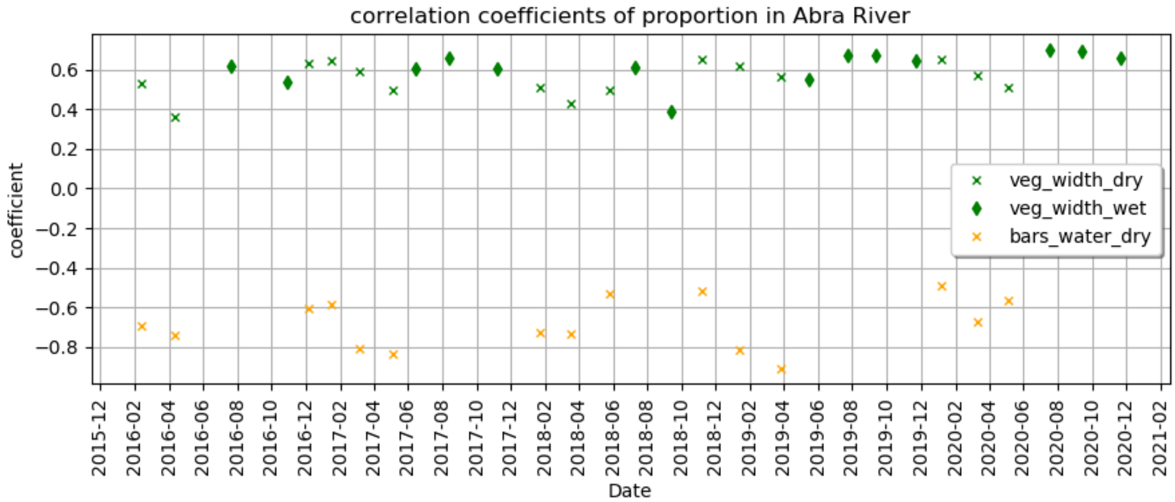

Figure S12. Abra River landforms' proportion- AW correlation coefficients time series.

Figure S13. Detection of morphology change (in red and blue circle) between 2020 and 2021 in sub reach 2 of Abra River.

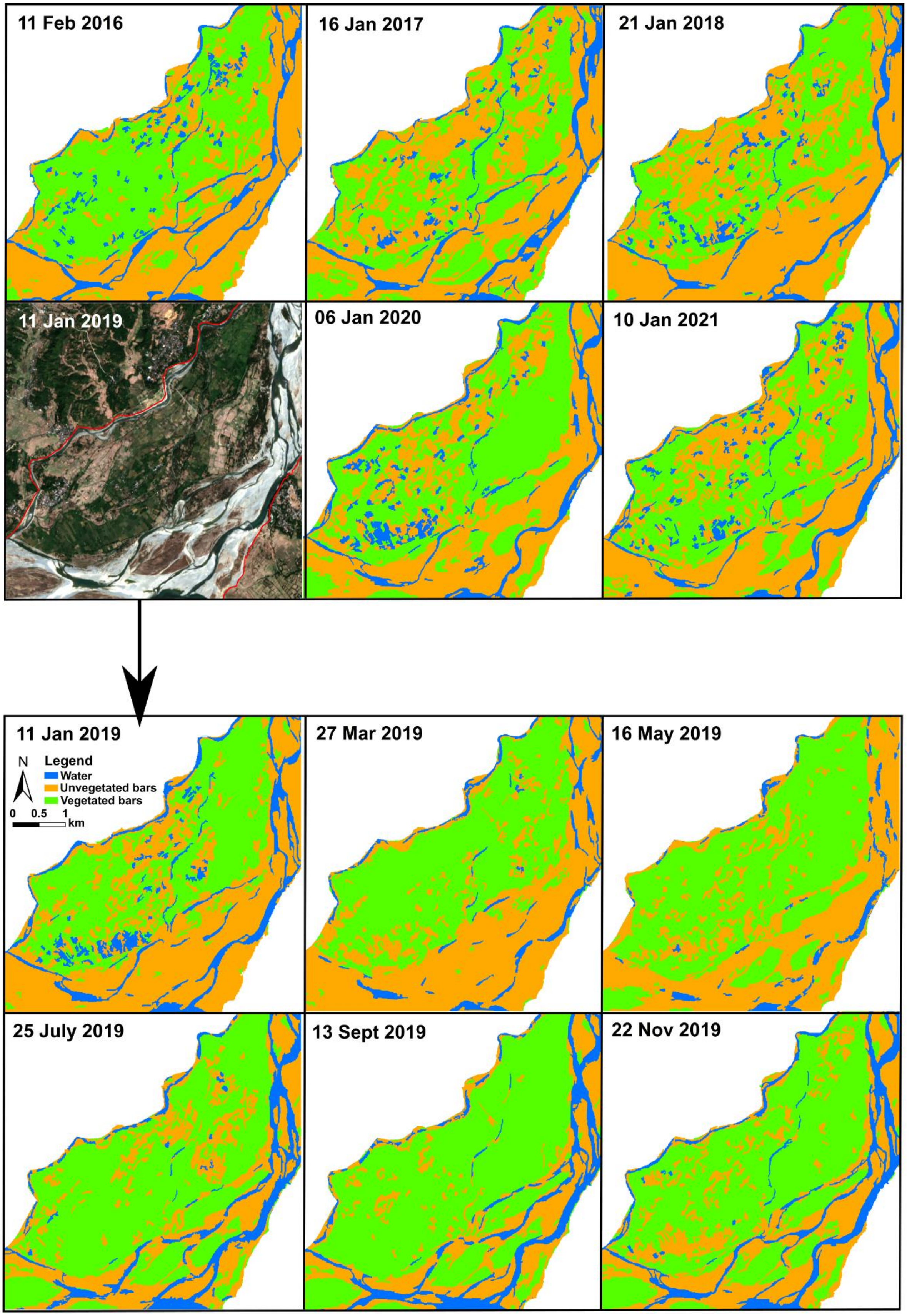

1349 Figure S14. Mapped morphologic seasonal change and yearly change in a
1350 sub-reach of Abra River.